



Tracking vegetation phenology of pristine northern boreal peatlands by combining digital photography with CO₂ flux and remote sensing data

Maiju Linkosalmi¹, Juha-Pekka Tuovinen¹, Olli Nevalainen¹, Mikko Peltoniemi³, Cemal M. Taniş², Ali N. Arslan², Juuso Rainne¹, Annalea Lohila¹, Tuomas Laurila¹, Mika Aurela¹

¹Finnish Meteorological Institute, Helsinki, Climate System Research, 00560 Helsinki, Finland

²Finnish Meteorological Institute, Helsinki, Arctic Space Centre, 00560 Helsinki, Finland

³Natural Resources Institute Finland (LUKE), 00790 Helsinki, Finland

Correspondence to: Maiju Linkosalmi (maiju.linkosalm@fmi.fi)

Abstract. Vegetation phenology, which refers to the seasonal changes in plant physiology, biomass and leaf area, is affected by many abiotic factors, such as precipitation, temperature and water availability. Phenology is also associated with the carbon dioxide (CO₂) exchange between ecosystems and the atmosphere. We employed digital cameras to monitor the vegetation phenology of three northern boreal peatlands during five growing seasons. We derived a greenness index (Green Chromatic Coordinate, GCC) from the images and combined the results with measurements of CO₂ flux, temperature and water table level, and with high-resolution satellite data (Sentinel-2). From the digital camera images it was possible to extract greenness dynamics on the vegetation community and even species level. The highest GCC and daily maximum gross photosynthetic production (GPP_{max}) were observed at the site with the highest nutrient availability and richest vegetation. The short-term temperature response of GCC depended on temperature and varied among the sites and months. Although the seasonal development and year-to-year variation of GCC and GPP_{max} showed consistent patterns, the short-term variation in GPP_{max} was explained by GCC only during limited periods. GCC clearly indicated the main phases of the growing season and peatland vegetation showed capability to fully compensate for the impaired growth resulting from a late growing season start. The GCC data derived from Sentinel-2 and digital cameras showed similar seasonal courses, but a reliable timing of different phenological phases depended upon the temporal coverage of satellite data.

1 Introduction

Boreal peatlands constitute a major terrestrial carbon (C) storage and continuously accumulate more C as a result of restricted decomposition of organic matter in anaerobic conditions. Boreal peatlands cover about 3% of the total land area, but they account for as much as a third of the global C pool (Gorham, 1991; Turunen et al., 2002). Climate and land use changes may disturb the functioning of these ecosystems and affect their exchange of carbon dioxide (CO₂) and other greenhouse gases (GHGs) with the atmosphere. Vegetation phenology, i.e. the seasonal changes in plant physiology, biomass and leaf area (Migliavacca et al., 2011; Sonnentag et al., 2011; Sonnentag et al., 2012; Bauerle et al., 2012), is one of the drivers of the C cycle of terrestrial ecosystems and is strongly linked to plant productivity and CO₂ exchange (Ahrends et al., 2009; Peichl et al., 2015; Toomey et al., 2015; Linkosalmi et al., 2016; Koebisch et al., 2019). Abiotic factors, such as precipitation, temperature, radiation and water availability, act as main drivers of ecosystem functioning and vegetation phenology (Bryant and Baird, 2003; Körner and Basler, 2010). Earlier onset of vegetation growth during the springtime, and thus a longer growing season, has been observed in recent decades in the boreal zone (Linkosalo, et al. 2009; Delbart et al., 2008; Nordli et al., 2008; Pudas et al., 2008). This strongly affects the annual C balance of ecosystems, because C accumulation starts as soon as environmental conditions become favourable for photosynthesis



and growth. In contrast, the corresponding lengthening in autumn does not have a similar effect (Goulden et al., 1996; Berninger, 1997; Black et al., 2000; Barr et al., 2007; Richardson et al., 2009), as also ecosystem respiration increases in late summer and autumn (White and Nemani, 2003; Dunn et al., 2007). In peatlands, the relationship between vegetation phenology and CO₂ exchange has been verified in several studies (Järveoja et al., 2018; Koebsch et al., 2019; Peichl et al., 2015; Peichl et al., 2018; Linkosalmi et al., 2016; Knox et al., 2017).

Remote sensing, both ground and satellite-based, is an effective tool for continuous monitoring of vegetation phenology and, thus, indirectly C fluxes. Time-lapse imaging with ground-based digital cameras provides small-scale information on the changes in the vegetation observed, even on the species and vegetation community level. Several studies have shown that such repeat photography is capable of detecting the key patterns and events of vegetation phenology and it is possible to relate these observations to variations in CO₂ exchange (e.g. Wingate et al., 2015; Richardson et al., 2007; Richardson et al., 2009; Linkosalmi et al., 2016; Peichl et al., 2015; Koebsch et al., 2019). Especially, the Green Chromatic Coordinate (GCC) extracted from the red-green-blue (RGB) colour channel information of digital images has been used as an index of canopy greenness (e.g. Richardson et al., 2007; Richardson et al., 2009; Ahrends et al., 2009; Ide et al., 2010; Sonnentag et al., 2012; Peichl et al., 2015; Peltoniemi et al., 2018).

Satellite data offer many benefits for land cover mapping: the data are cost-effective, cover large areas, and even the most remote sites are accessible (e.g. Lees et al., 2018). However, the vegetation and microtopography at many peatland sites are heterogeneous, which complicates the interpretation of satellite data. Furthermore, the presence of both vascular plants and mosses can be challenging for satellite-based monitoring, as the species have different heights and cover each other forming an understory and other vegetation layers. The microtopography depends on the peatland type, and the surface can be relatively flat or patterned with strings and flarks.

In this study, vegetation phenology was observed with digital cameras in three natural peatlands in northern Finland for five growing seasons. Our specific aims were to examine (1) how the GCC describes the variation of vegetation phenology between the sites and among different plant communities within one site, including the relationship between vegetation phenology and CO₂ flux dynamics, (2) how the abiotic factors (temperature, water table depth) modulate the development of GCC and CO₂ flux and (3) the potential use of satellite-derived GCC data for depicting the phenology of northern peatlands.

2 Material and methods

2.1 Sites

The three study sites are natural open peatlands, all located in northern Finland. Halssiaapa in Sodankylä (N67°22.117', E26°39.244', 180 m a.s.l.) is the southernmost of the sites and, as a mesotrophic fen, represents a typical aapa mire. The vegetation mainly consists of sedges (*Carex* spp.), big-leafed bogbean (*Menyanthes trifoliata*), bog-rosemary (*Andromeda polifolia*), dwarf birch (*Betula nana*), cranberry (*Vaccinium oxycoccos*) and peat moss (*Sphagnum* spp.). Tall trees are not present, only some minor downy birch (*B. pubescens*) and Scots pine (*Pinus sylvestris*). Different types of vegetation are located on drier strings (shrubs) and wetter flarks (sedges and herbs). The trophic status varies from oligotrophic to eutrophic.

Lompolojänkkä (N67°59.842', E24°12.569', 269 m a.s.l.) is a nutrient-rich sedge fen located in the Pallas area. Of our study sites, Lompolojänkkä is the richest in nutrients. This is reflected in the vegetation, which is dominated by *B. nana*, *Menyanthes trifoliata*,



75 downy willow (*Salix lapponum*), *Carex* spp. and *Sphagnum* and brown mosses (Aurela et al., 2009). Lompolojänkki has the highest leaf area index (one-sided LAI of 1.3 m² m⁻²) (Aurela et al., 2009).

Kaamanen (N69°08.435', E27°16.189', 155 m a.s.l.) is the northernmost of the sites and also represents an aapa mire. The site is located within the northern boreal vegetation zone, but the climate is already subarctic (Aurela et al., 1998). Vegetation is distributed to wet flarks and strings of 0.3–0.6 m in height. On the strings, the vegetation mainly consists of ombrotrophic species, such as forest mosses and Ericales (Maanavilja et al., 2011). *Sphagnum* mosses, sedges, *B. nana* and *Andromeda polifolia* dominate the margins of the strings. The flarks are dominated by meso-eutrophic vegetation, such as brown mosses and sedges (Maanavilja et al., 2011). Of these sites, the LAI is lowest (0.7 m² m⁻²) at Kaamanen. At all sites, the snowmelt typically occurs in May.

2.2 Image analysis

85 The images were taken with StarDot Netcam SC 5 digital cameras and cover the years from 2015 to 2019. The cameras were placed in a weatherproof housing and attached to line current and a remote web server. Images were taken automatically every 30 minutes with a 2592x1944 resolution in 8-bit JPEG format and transferred automatically to the server. The cameras were adjusted in an angle of 45° on a pole facing the north. The cameras were mostly observing the peatland vegetation, but also the skyline was visible in the images. The image quality settings (saturation, contrast and color balance) were the same in all cameras.

90

The data gained from the digital camera images consist of colour-based chromatic indices. The images were analyzed with the FMIPROT (version 0.21.1) program that was designed as a toolbox for image processing for phenological and meteorological purposes (Tanis et al., 2018). FMIPROT automatically derives the colour fraction indices from the images. We used the Green Chromatic Coordinate (GCC):

$$95 \quad GCC = \frac{\Sigma G}{\Sigma R + \Sigma G + \Sigma B} \quad (1)$$

where ΣG , ΣR , ΣB are the sums of green, red and blue channel indices, respectively, of all pixels comprising an image. In FMIPROT it is possible to choose different subareas, Regions of Interest (ROIs), within the image, for which GCC is calculated separately. At the latitude of our study sites, solar radiation levels have been observed to be sufficient for image analysis from February to October and the diurnal radiation levels acceptable from 11:00 to 15:00 (local winter time, +02:00 GMT) (Linkosalmi et al., 2016).

100 Here, we used images from the beginning of May to the end of September, which represent the growing season, and daily GCC averages were calculated from the images taken during 11:00–15:00.

2.3 Regions of interest (ROIs)

The ROIs covering all different plant communities within the target area of the camera were defined for each site (Fig. 1 a-c). In addition to these general ROIs, more specific ROIs (Fig. 1 d-f) were defined for clearly identifiable plant communities characterized by specific dominant plant species (Table 1).

105

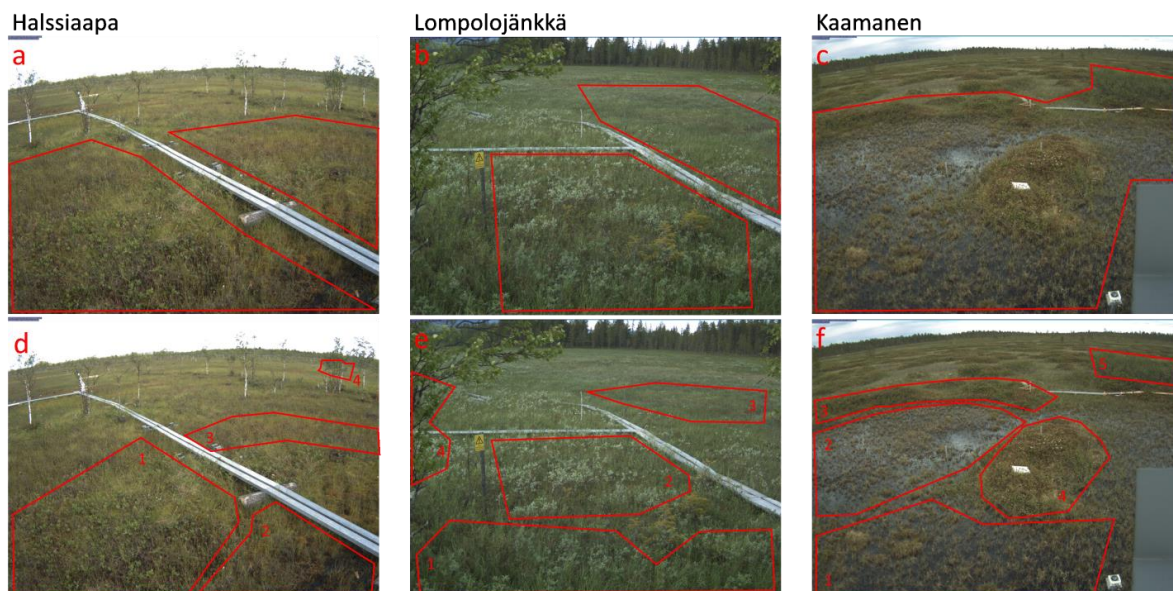


Figure 1: The Region of Interests (ROIs) representing the overall vegetation at the site (a-c) and specific plant communities within the camera target areas (d-f). The numbers 1-5 indicate the plant communities detailed in Table 1.

Table 1: The dominant plant species characterizing the different plant communities within Region of Interests (ROIs) at each site (Fig. 1 d-f).

	Halssiaapa	Lompolojänkkä	Kaamanen
ROI1	<i>Menyanthes trifoliata</i>	<i>Salix</i> sp., <i>Carex</i> spp.	<i>Carex</i> spp. and flark mosses
ROI2	Sedges (mostly <i>Carex</i> spp.)	<i>Salix</i> sp., <i>Carex</i> spp.	<i>Carex</i> spp. and flark mosses
ROI3	<i>Andromeda polifolia</i> and other shrubs	<i>Carex</i> spp.	<i>Empetrum nigrum</i> , <i>Rubus chamaemorus</i>
ROI4	<i>Betula pubescens</i>	<i>Betula nana</i>	<i>Rhododendron tomentosum</i> , <i>Rubus chamaemorus</i>
ROI5			<i>Betula nana</i>

2.4 Ecosystem scale CO₂ exchange and meteorological observations

The ecosystem–atmosphere CO₂ exchange was measured by the micrometeorological eddy covariance (EC) method. The EC method provides continuous CO₂ flux data averaged on an ecosystem scale. The vertical CO₂ flux is defined as the covariance of the high-frequency (10 Hz) fluctuations of vertical wind speed and CO₂ mixing ratio. At each site, the EC measurement system consisted of a USA-1 (METEK GmbH, Elmshorn, Germany) three-axis sonic anemometer and a closed-path LI-7000 (Li-Cor., Inc., Lincoln, NE, USA) CO₂/H₂O gas analyzer. Air temperature, photosynthetic photon flux density (PPFD) and water table level were also measured at the sites. The measurement system and the data processing procedures have been presented in detail by Aurela et al. (2009).

120

The measured CO₂ flux represents the net ecosystem exchange (NEE), which is the sum of gross photosynthetic production (GPP) and ecosystem respiration. The daily maximum GPP, GPP_{max}, was calculated as the difference between the mean daytime (PPFD



> 600 $\mu\text{mol m}^{-2} \text{s}^{-1}$) and nighttime (PPFD < 20 $\mu\text{mol m}^{-2} \text{s}^{-1}$) NEE. The GPP_{max} describes the seasonal GPP cycle and also reacts to short-term changes in air temperature and humidity (Aurela et al., 2001).

125 2.5 Growing degree day sum, growing season start and temperature classes

Growing Degree Day Sum (GDDS) was defined as the cumulative sum of the daily average temperatures exceeding 5 °C, each subtracted with the base value of 5 °C. The growing season was considered to start when the daily mean temperature has remained over 5 °C for ten days. The short-term change in GCC was expressed as a mean three-day difference, i.e. $\Delta\text{GCC} = \text{GCC}(\text{day}_t) - \text{GCC}(\text{day}_{t+3})$. It was calculated throughout the five growing seasons, and its monthly average was divided into three temperature classes (<5 °C, 5-10 °C and >10 °C) calculated as a two-day average (day_t and day_{t+1}). Also, cumulative GCC was calculated using the value just before the increase as the baseline. The cumulative sums were normalized by the maximum and minimum values of the year with the maximum cumulative GCC.

130 2.6 Satellite data

The GCC derived from the digital images of the ground-based cameras was compared with those derived from the Sentinel-2 data
135 acquired from 2016 to 2019. GCC was computed from the atmospherically corrected bottom-of-atmosphere products (Level-2A) using bands B2 (blue, 490 nm), B3 (green, 560 nm) and B4 (red, 665 nm) with a 10 m spatial resolution. Level-2A products were downloaded from the Sentinel Scientific Data Hub (<https://scihub.copernicus.eu>). If the Level-2A product was not available for a specific date, the Level-1C product was downloaded and processed to Level-2A product using the Sen2Cor software (version 2.8). Cloudy, cloud-shadowed and snowy satellite images were filtered using the scene classification data (SCL Band) available in the
140 Level-2A products.

GCC was calculated for multiple ROIs within each site (Fig. 2). These ROIs were different from those used with camera data because of the different spatial resolutions of the camera and satellite data. The selected ROIs represent different vegetation types with different microtopography within the study areas. The average of pixel-based GCCs within a ROI was used as the ROI-based
145 GCC. Site-based GCC was then calculated as the average of all ROI-based GCCs within the site. The Sentinel-2 images were available at the minimum for every two days, but the filtering reduced the number of valid images.



150 **Figure 2: The Region of Interests (ROIs) representing the overall vegetation at the sites for the Sentinel-2 satellite images. The aerial photo contains data from the National Land Survey of Finland Topographic Database.**



2.7 Fitting of GCC and GPPmax cycles

To depict the phenology-driven seasonal cycle, we fitted a double hyperbolic tangent function to both camera- and satellite-derived GCC time series with the Levenberg-Marquardt least squares method (Meroni et al., 2014; Vrieling et al., 2018):

$$GCC(t) = a_0 + a_1 \frac{\tanh((t-a_2)a_3)+1}{2} + a_4 \frac{\tanh((t-a_5)a_6)+1}{2} - a_4, \quad (2)$$

155 where t is time, a_0 is the minimum GCC value at the start of the growing season, a_1 (a_4) is the difference between the maximum GCC and minimum GCC, a_2 (a_5) is the inflection point in GCC development, and a_3 (a_6) controls the slope at the inflection point in GCC development during the first (second) half of the growing season. A similar function was fitted to GPP_{\max} .

160 Visible snow included in the images affects the GCC data by overexposure. Thus, only the data collected after the snowmelt, which usually occurs in May at all sites, was used. Also, the starting point of the fits was fixed to 1 May (Day of Year (DOY) 121), and the GCC value for this day was calculated as the average of the yearly minima after the snowmelt, whose timing was specified for each year and site. Likewise, the growing season ends by the end of October, and thus the end point of the fit was fixed to 31 October (DOY 304), for which GCC was determined by averaging annual minima in the end of the growing season.

165 From the fitted function, we calculated parameters that describe phenological phases and vegetation development. These parameters were chosen as the start of season (SOS25), which stands for 25% of the GCC difference between the maximum and 1 May, maximum GCC (MAX) and the end of season (EOS25), defined as 25% of the GCC difference between 30 October and the maximum.

2.8 Statistical analysis

170 The differences in GCC between the sites, different plant communities and measurement years were tested with the Kruskal-Wallis one-way analysis of variance on ranks for the group-wise comparison. Dunn's test was used for post-hoc testing. The Kruskal-Wallis method was used due to the non-normal distribution of the seasonal GCC data. The presence of autocorrelation in the residuals of the regression between GCC and GPP_{\max} was verified with the Durbin-Watson test. Autocorrelation was eliminated by regressing the first differences of the data, i.e. by applying the transformation $x'_t = x_t - x_{t-1}$ where x_t and x_{t-1} are consecutive
175 observations. The statistical analyses were performed with the R software (version 4.0.5).

3 Results

3.1 Greenness variation

The seasonal development of vegetation during the growing season could be visually observed from the imagery collected at our study sites, as exemplified by Figure 3. The spring development, greening and senescence of vegetation during the growing season
180 were visible in the images, and so were the changes in the areas covered by surface water.

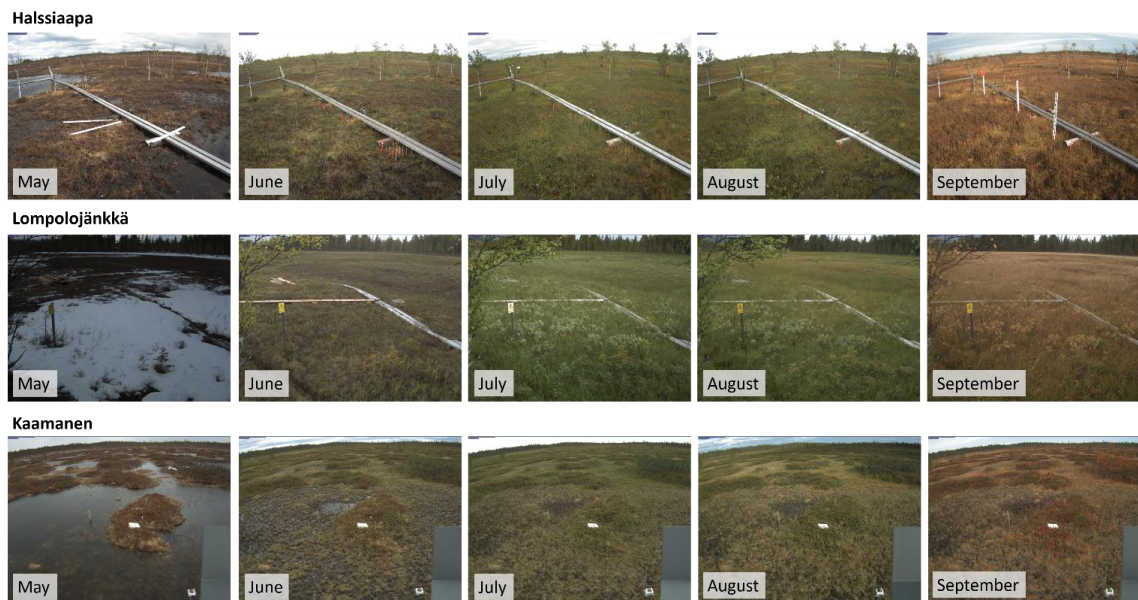
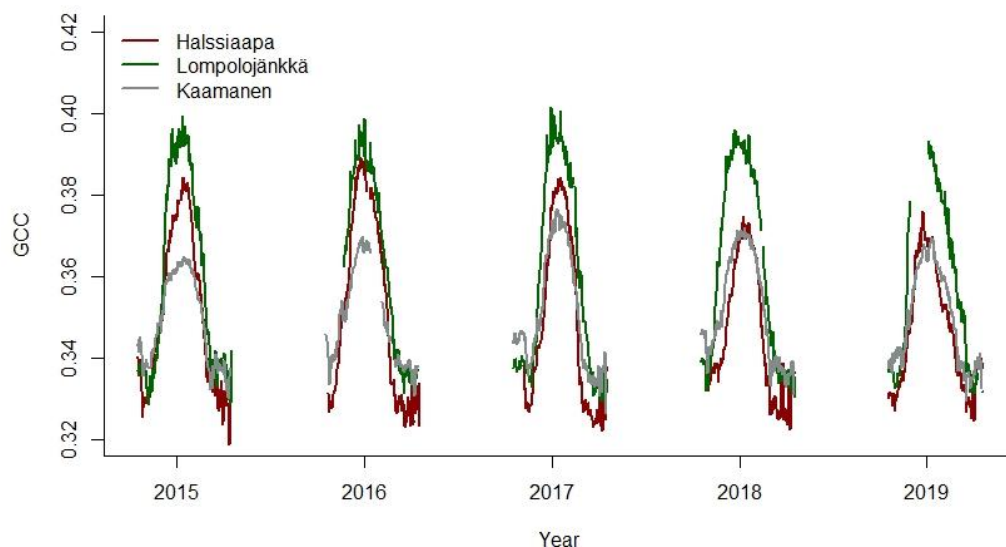


Figure 3: The seasonal development of vegetation and surface water from May to September in 2015 at Halssiaapa, Lompolojänkkä and Kaamanen. The pictures were taken on the 15th of each month, with the exception of the 17th of June at Kaamanen.

185 The mean growing season GCC values obtained from the phenological cameras showed that Lompolojänkkä systematically had the highest GCC values over the five growing seasons (Fig. 4 and Appendices Fig. A4). In 2015 and 2016, there was a significant difference ($p < 0.05$) in GCC between Lompolojänkkä and the other two sites. In 2017, 2018 and 2019, the pairwise comparison showed a significant ($p < 0.05$) difference in GCC between all the sites. The maximum GCC during the whole study period of 2015–2019 was observed in 2017 at Lompolojänkkä and Kaamanen and in 2016 at Halssiaapa (Fig. 4, Table 2).



190

Figure 4: Daily camera-based GCC values from 1 May to 30 September in 2015–2019.



Table 2: The mean GCC and GPPmax during the week they attained the maximum, the week numbers of these maxima and the week number of the growing season (GS) start. The GCC data from Lompolojänkkä and GPPmax data from Kaamanen from 2019 are missing.

Halssiaapa

	Max GCC	Max GCC week	Max GP	Max GP week	GS start week
2015	0.383 ± 0.018	31	0.318 ± 0.097	30	22
2016	0.388 ± 0.022	27	0.353 ± 0.108	27	18
2017	0.383 ± 0.020	31	0.338 ± 0.123	32	23
2018	0.371 ± 0.016	29	0.257 ± 0.090	32	19
2019	0.372 ± 0.015	27	0.302 ± 0.073	28	21

Lompolojänkkä

	Max GCC	Max GCC week	Max GP	Max GP week	GS start week
2015	0.396 ± 0.024	31	0.520 ± 0.184	31	22
2016	0.394 ± 0.020	27	0.551 ± 0.185	27	20
2017	0.397 ± 0.024	29	0.563 ± 0.209	31	23
2018	0.394 ± 0.022	27	0.498 ± 0.181	30	19
2019		-	0.555 ± 0.197	29	22

Kaamanen

	Max GCC	Max GCC week	Max GP	Max GP week	GS start week
2015	0.364 ± 0.010	31	0.299 ± 0.094	30	22
2016	0.368 ± 0.011	29	0.297 ± 0.089	28	19
2017	0.376 ± 0.014	30	0.335 ± 0.116	29	23
2018	0.371 ± 0.012	29	0.261 ± 0.090	32	19
2019	0.369 ± 0.012	30	-	-	22

195

There were significant GCC differences among different plant communities at all sites ($p < 0.05$), except in 2017 at Halssiaapa and Kaamanen (Appendices Table A1). In general, at all sites the GCC of birch species (*Betula pubescens* and *B. nana*) differed significantly from the other plant species. At Halssiaapa, the plant communities with sedges (*Carex spp.*) and shrubs (e.g. *Andromeda polifolia*) differed from annuals with bigger leaves, such as *Menyanthes trifoliata*. At Kaamanen, the shrubs and annuals (e.g. *Empetrum nigrum*, *Rhododendron tomentosum*, *Rubus chamaemorus*) had a significantly higher GCC than the plant communities with sedges and flark mosses. The comparison of the maximum GCC values of different plant communities, calculated as weekly means, supported these results as the annuals and woody plants with relatively large leaves, such as *Menyanthes trifoliata*, *Rubus chamaemorus*, *Salix spp.* and *Betula spp.*, generated a higher GCC maximum than *Carex spp.* and shrubs (Table 3). At Halssiaapa, the highest maximum GCC during 2015–2017 and 2019 was observed in ROI1, which is dominated by *Menyanthes trifoliata*, whereas in 2018 the highest GCC was found for ROI3, an area with *Andromeda polifolia* and other shrubs. At Lompolojänkkä, the highest annual GCC maximum was consistently observed in a plant community dominated by *Salix sp.* and *Carex spp.* (ROI1). Most likely the ground layer with mosses and dead plant material reduced the GCC within those ROIs that had sparse vegetation. Among the measurement years, most plant communities at Halssiaapa showed the highest maximum GCC in 2016. At Lompolojänkkä, the maximum GCC of different ROIs varied between the years 2015, 2016 and 2017, while at Kaamanen all plant communities attained their maxima in 2017.

200
205
210



215 **Table 3: The maximum GCC values of different plant communities characterized by the dominant species specified in Table 1 (defined as image ROIs) from 2015 to 2019. The maximum value among different ROIs is marked as bold, and the maximum among the years is underlined. The ROIs are described in Section 2.4. The data from Lompolojännkä are missing in 2019.**

Halssiaapa					
	ROI1	ROI2	ROI3	ROI4	
2015	0.387 ± 0.019	0.373 ± 0.016	0.376 ± 0.018	0.372 ± 0.016	
2016	<u>0.391 ± 0.023</u>	<u>0.378 ± 0.019</u>	<u>0.382 ± 0.021</u>	0.371 ± 0.015	
2017	0.384 ± 0.020	0.358 ± 0.018	0.381 ± 0.021	<u>0.372 ± 0.016</u>	
2018	0.370 ± 0.015	0.365 ± 0.014	0.374 ± 0.018	0.370 ± 0.013	
2019	0.374 ± 0.015	0.366 ± 0.013	0.368 ± 0.014	0.371 ± 0.013	

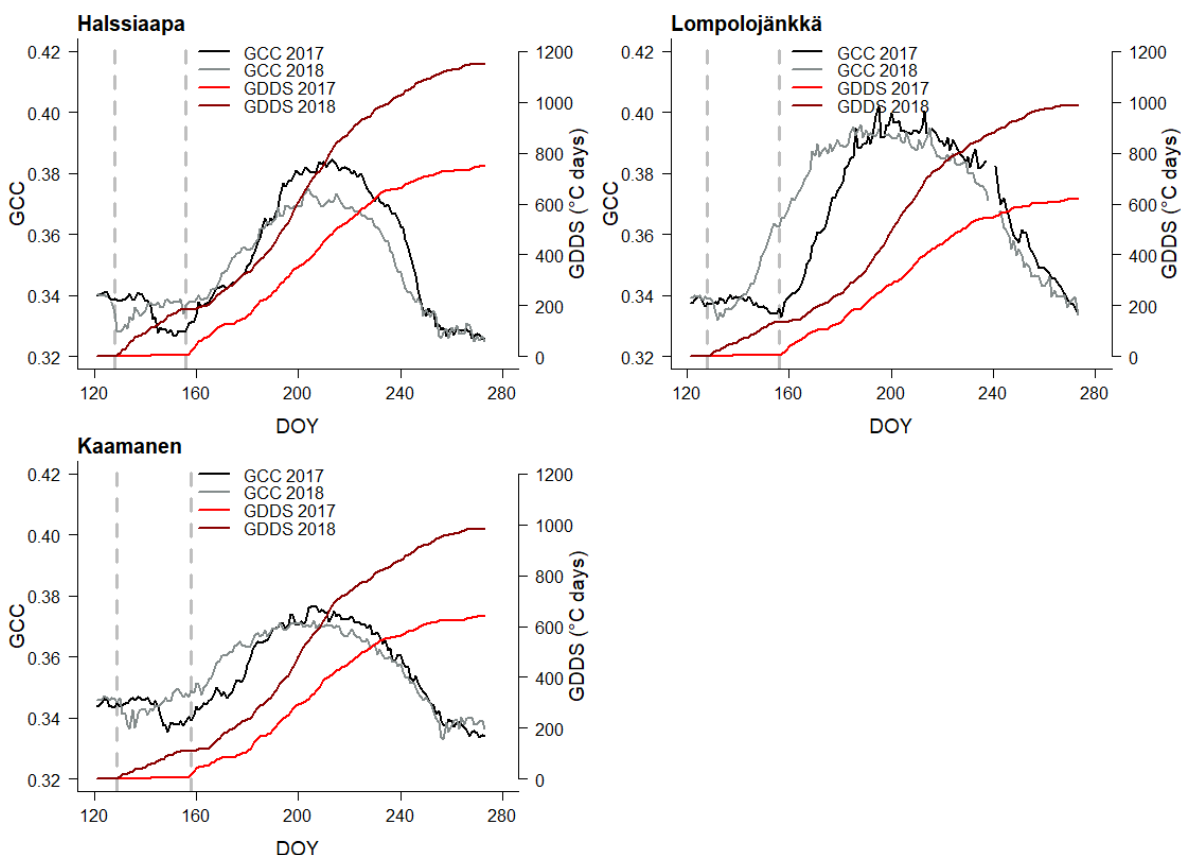
Lompolojännkä					
	ROI1	ROI2	ROI3	ROI4	
2015	<u>0.406 ± 0.027</u>	<u>0.395 ± 0.024</u>	0.388 ± 0.022	<u>0.403 ± 0.026</u>	
2016	0.400 ± 0.019	0.393 ± 0.022	<u>0.396 ± 0.021</u>	0.397 ± 0.024	
2017	<u>0.406 ± 0.027</u>	0.393 ± 0.023	<u>0.396 ± 0.023</u>	0.402 ± 0.027	
2018	0.401 ± 0.023	0.392 ± 0.022	0.393 ± 0.022	0.400 ± 0.024	
2019	-	-	-	-	

Kaamanen					
	ROI1	ROI2	ROI3	ROI4	ROI5
2015	0.358 ± 0.008	0.357 ± 0.007	0.376 ± 0.016	0.375 ± 0.016	0.374 ± 0.019
2016	0.363 ± 0.009	0.362 ± 0.008	0.380 ± 0.016	0.379 ± 0.016	0.377 ± 0.017
2017	<u>0.371 ± 0.011</u>	<u>0.368 ± 0.010</u>	<u>0.384 ± 0.019</u>	0.388 ± 0.021	<u>0.385 ± 0.019</u>
2018	0.365 ± 0.009	0.365 ± 0.009	0.379 ± 0.015	0.381 ± 0.017	0.378 ± 0.016
2019	0.363 ± 0.008	0.362 ± 0.007	0.379 ± 0.015	0.377 ± 0.015	0.378 ± 0.016

3.2 Temperature and GCC development

220 The relationship between temperature and GCC was examined by creating normalized cumulative GCC and GDDS curves for all the growing seasons (Appendices Fig. A4). The cumulative sums show that the GCC started to accumulate later than GDDS. In 2017, the snow cover lasted at all sites until the beginning of June, which delayed the GDDS development and the start of the growing season compared to the other study years (Figs. 5 and 7 and Appendices Figs. A3 and A4). Consequently, GCC did not increase until the beginning of June (4 June in Halssiaapa and Lompolojännkä and 7 June in Kaamanen), when the snow was melted. Despite the slow start of growth in 2017, the peatland vegetation was capable of catching up its typical development, and 225 at Lompolojännkä and Kaamanen GCC even reached the highest summer maximum during the study years (Table 2).

During the measurement years, warmer springs and thus earlier snowmelts resulted in an earlier green-up of vegetation. No clear connection between the growing season start and the timing of the maximum of either GCC or GPP_{max} was found at Lompolojännkä or Kaamanen (Table 2). At Halssiaapa, however, the earliest growing season start, the maximum value and the earliest timing of both GCC and GPP_{max} occurred in the same year, 2016. During our study period, the year 2018 had the warmest summer at all sites (Appendices Figs. A2 & A3). At Halssiaapa, the water table depth increased substantially during the growing seasons of 2018 and 2019 as a result of drought (Appendices Fig. A2). The same was true at Kaamanen (data missing in 2019), while at Lompolojännkä WTD was not affected. The effect of drought is also visible in the daily and cumulative GCC values (Fig. 4 and Appendices Fig. A4).



235

Figure 5: Development of GCC and growing degree day sum (GDDs) from 1 May to 30 September at Halssiaapa, Lompolojänkkä and Kaamanen. The years 2017 and 2018 are shown here as an example of a cold and warm spring, respectively. The grey dashed lines indicate the start of the growing season.

240 The short-term GCC change ΔGCC , expressed here as the monthly mean 3-day difference, depended on both the month and temperature range (Fig. 6). In May, this change, which is indicative of vegetation development, was substantially smaller for temperatures below than above 5 °C. No significant ($p < 0.05$) differences were found between the sites, nor during any month in the lowest temperature class (Fig. 6). At Lompolojänkkä, ΔGCC started at a lower temperature and was generally larger than at the other sites. The vegetation growth in June at Halssiaapa seemed to benefit from temperatures over 10 °C, while at Lompolojänkkä this limit was lower. At Kaamanen, however, the ΔGCC in June was similar in all temperature classes. In July, GCC started to stabilize and a significant positive change was only observed at Kaamanen for temperatures between 5 and 10 °C and at Halssiaapa with temperatures over 10 °C. In August and September, ΔGCC was negative due to senescence (Fig. 6). The ΔGCC of different plant communities (Appendices Fig. A5) showed that the growth of *Betula spp.* started strong in May at all sites, but in June the birches already had a lower ΔGCC than other plant communities. The highest plant community-specific ΔGCC values were found at Lompolojänkkä, which was consistent with the spatially averaged ΔGCC data (Figs. 4 & 6).

245

250

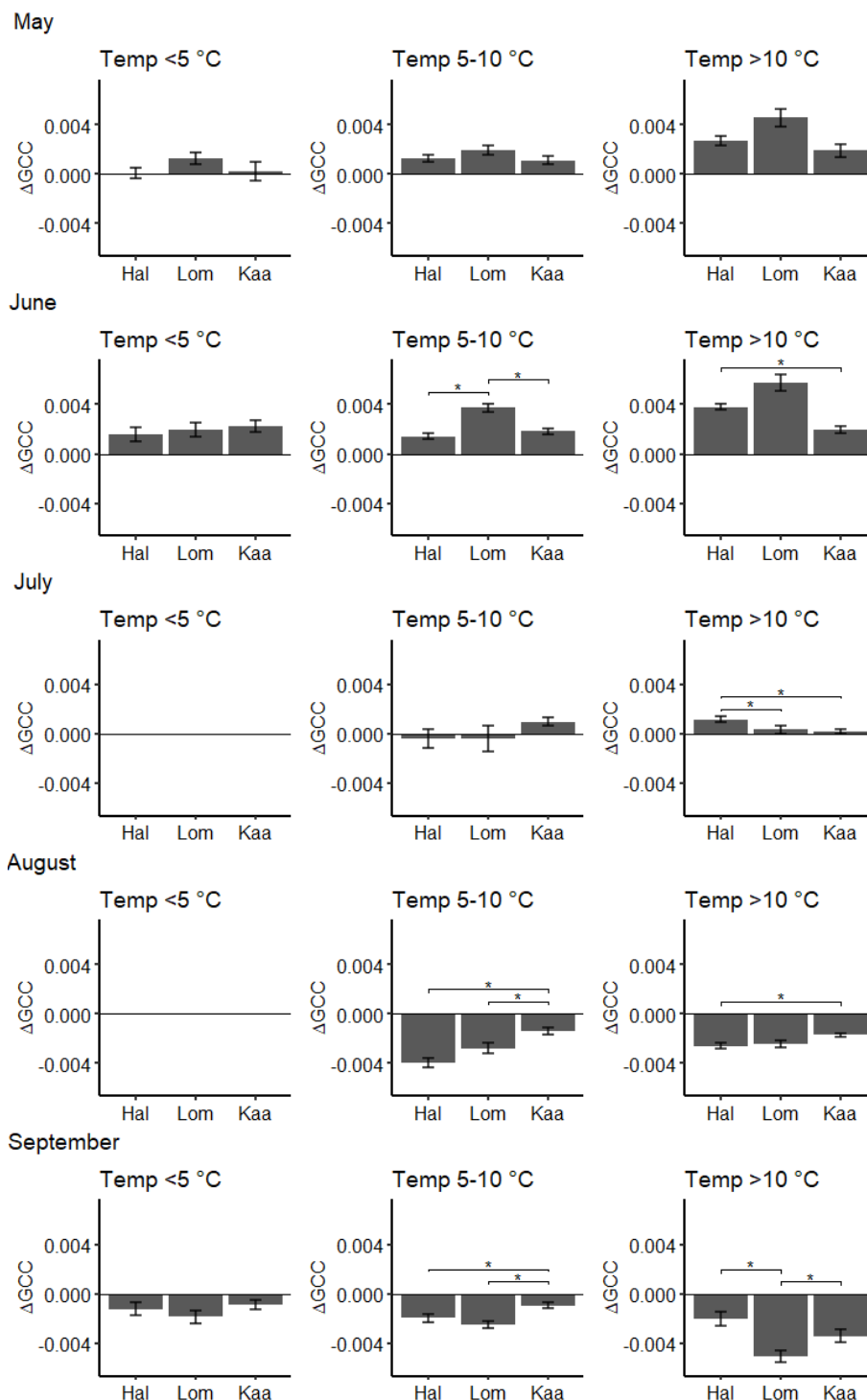


Figure 6: Mean three-day difference in GCC divided to temperature classes (<math><5\text{ }^\circ\text{C}</math>, $5\text{-}10\text{ }^\circ\text{C}$, $>10\text{ }^\circ\text{C}$) at Halssiaapa (Hal), Lompoloj nkk  (Lom) and Kaamanen (Kaa) from May to September. There are no temperature data in the <math><5\text{ }^\circ\text{C}</math> class in July and August. The error bars denote the standard error, and the asterisks denote the statistically significant ($p < 0.05$) difference between the sites.

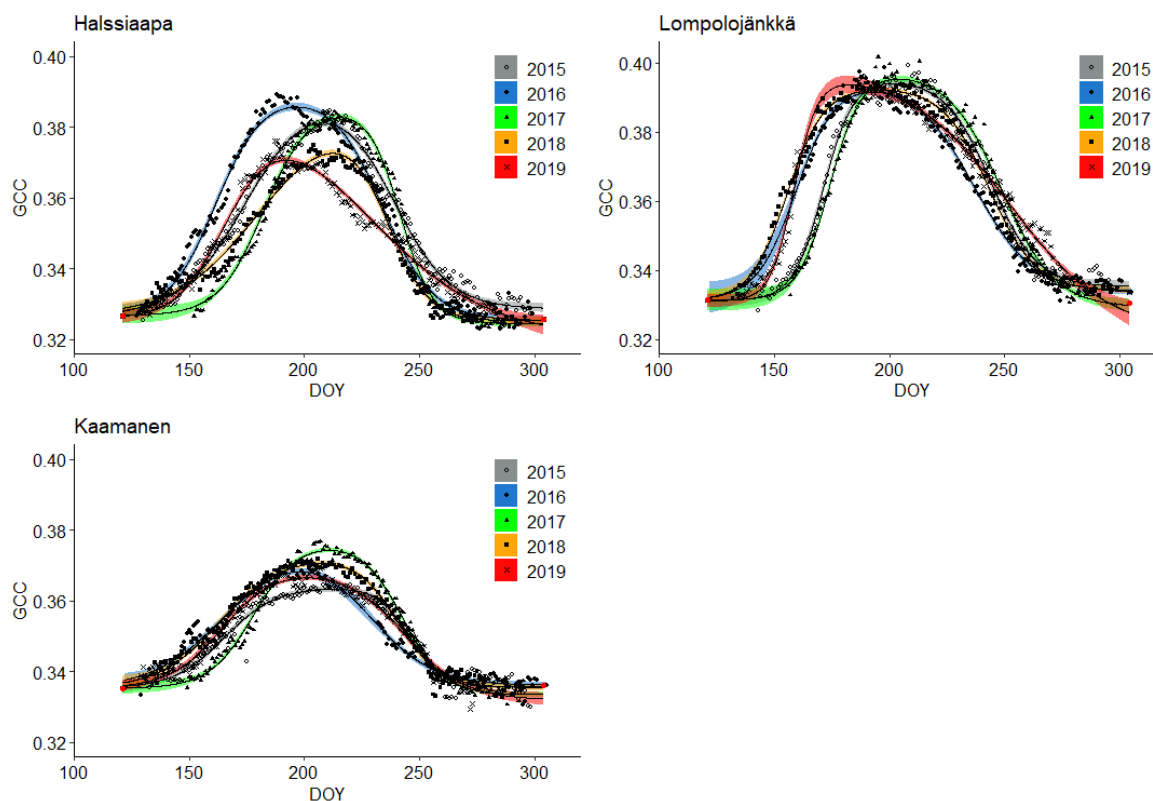
255



3.3 Seasonal GCC and GPP_{max} development

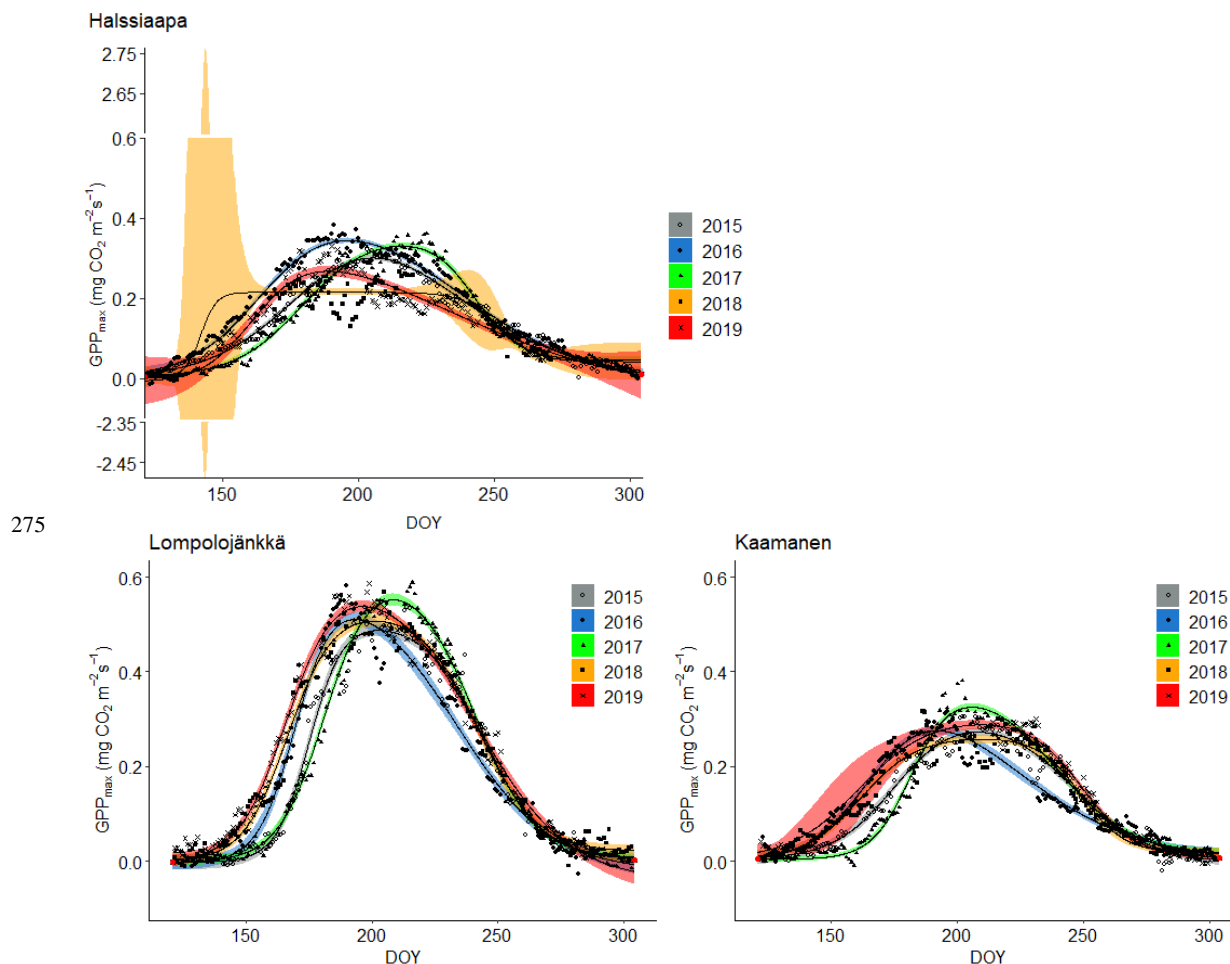
The start and end of the growing season were clearly visible in both the GCC and GPP_{max} data, which showed the same seasonal pattern (Figs. 7 & 8). As mentioned above, in 2017 the snow cover lasted until the beginning of June, which delayed the start of photosynthesis and thus vegetation development. At Halssiaapa, the year 2018 was hot and dry (Appendices Fig. A2), and this was reflected in the GCC and GPP_{max} data that were lower than in other years (Fig. 7 & 8). The GPP_{max} data were sparse during the growing season of 2018, which impaired the fit (Fig. 8). During the study period, the highest values of both GCC and GPP_{max} were observed in 2016 at Halssiaapa and in 2017 at Kaamanen and Lompolojänkkä (Figs. 7 & 8). In general, Lompolojänkkä had the highest GPP_{max}, GCC and LAI (Figs. 4, 7 and 8).

The difference in GCC was significant ($p < 0.05$) between Lompolojänkkä and the other two sites in all years, and in 2017, 2018 and 2019 also between Halssiaapa and Kaamanen. In 2015, GPP_{max} showed no difference among the sites, but in 2016 and 2019 there was a significant difference between Kaamanen and the other two sites, and in 2017 and 2018 between Lompolojänkkä and Kaamanen. The GPP_{max} and GCC showed a similar course throughout the growing season (Appendices Fig. A9).



270

Figure 7: Development of GCC from 1 May to 30 September in 2015–2019 at Halssiaapa, Lompolojänkkä and Kaamanen. Different symbols and colours denote different years, and the bands show the 95% confidence intervals of the fitted double hyperbolic tangent function. The red dots indicate the fixed start and end days defined for the fitting.



275

280

Figure 8: Development of GPP_{max} from 1 May to 30 September in 2015–2019 at Halssiaapa, Lompolojänkkä and Kaamanen. Different symbols and colours denote different years, and the bands show the 95% confidence intervals of the fitted double hyperbolic tangent function. The red dots indicate the fixed start and end days defined for the fitting. Note the differences in y-axis scaling.

A linear relationship between GCC and GPP_{max} was observed during both the increasing and decreasing phases of GCC (Table 4, Appendices Fig. A8). However, the Durbin-Watson test indicated that there was significant and strong autocorrelation in the model residuals. After differencing the data, the coefficient of determination was generally close to zero. There were periods showing correlated short-term variation in GCC and GPP_{max}, for example, at Kaamanen from late May to mid-June in 2016 and in June 2017 (Appendices Fig. A9 c), but most of the common variation in GPP_{max} and GCC was associated with the common seasonal cycle (Table 4).

285

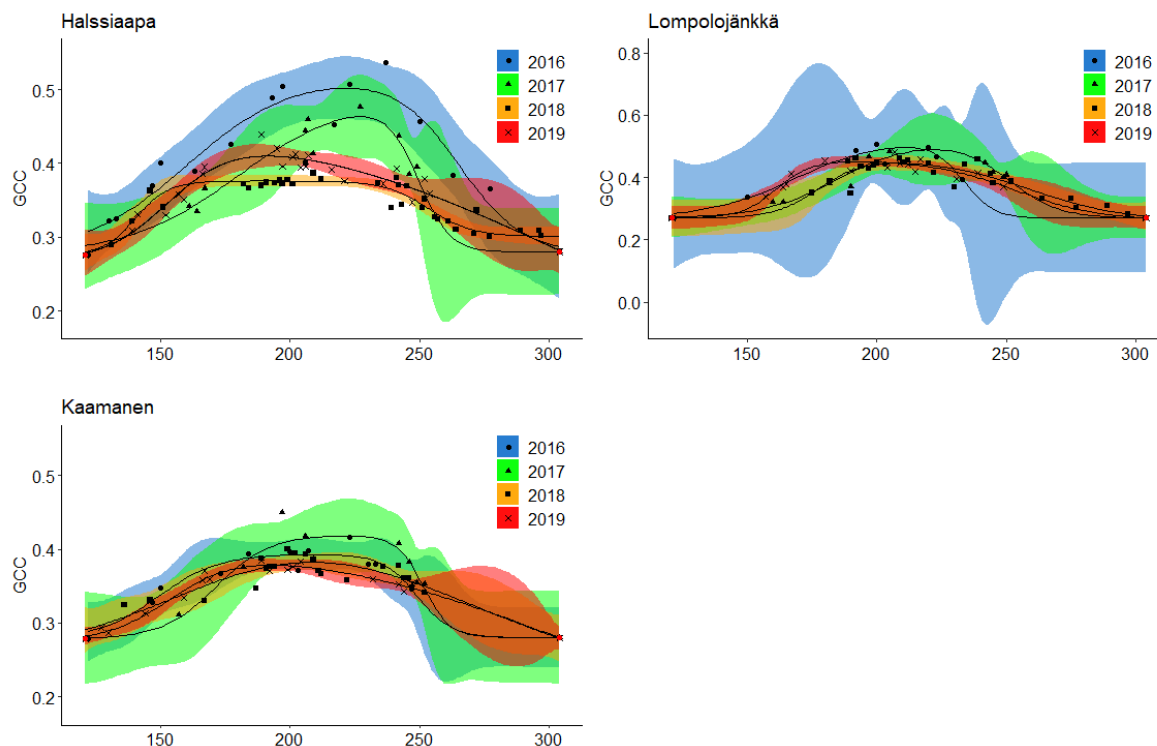


290 **Table 4: The coefficient of determination (R^2) of the linear regression between GCC and GPPmax and of the regression after differencing the data for autocorrelation. Letters a and b refer to the period before and after the annual GCC maximum, respectively.**

	Halssiaapa		Lompolojänkkä		Kaamanen	
	Original R^2	Autocorr. corr. R^2	Original R^2	Autocorr. corr. R^2	Original R^2	Autocorr. corr. R^2
2015 a	0.9749	0.0291	0.9549	0.0055	0.9372	0.0002
2015 b	0.9305	0.0015	0.9697	0.0082	0.9134	0.0023
2016 a	0.9848	0.0020	0.8668	0.1096	0.9304	0.0002
2016 b	0.9660	0.0112	0.9686	0.0001	0.8749	0.0001
2017 a	0.9448	0.0133	0.9599	0.3100	0.9171	0.0195
2017 b	0.9634	0.0550	0.9697	0.0138	0.9724	0.0065
2018 a	0.4468	0.0860	0.8890	0.1413	0.8944	0.0101
2018 b	0.9388	0.0088	0.9840	0.0119	0.9029	0.0045
2019 a	0.8513	0.0473	0.9162	0.0124	0.9854	0.1621
2019 b	0.8198	0.0024	0.9621	0.0011	0.9394	0.0570

3.4 Comparison between digital camera- and satellite-derived GCC

295 The retrieved GCC from the Sentinel-2 images had the same seasonal pattern as the camera-derived GCC (Fig. 9). Due to the sparseness of satellite data, however, the uncertainties were greater, as shown by the wider confidence intervals. The later season start and GCC maximum in 2017 at all sites and the lower GCC at Halssiaapa in 2018, compared to the other measurement years that were observed with cameras, were visible in the satellite-derived GCC. The GCC values from Sentinel-2 were in general higher than the camera-based GCC, which is most probably due to the different viewing angles and atmospheric effect (the scattering and absorption of radiation due to atmospheric molecules and aerosols) and the consequent atmospheric correction of
 300 the satellite data.



305 **Figure 9: Mean GCC derived from the Sentinel-2 data from 1 May to 30 September in 2016–2019 at Halssiaapa, Lompolojänkkä and Kaamanen. Different symbols and colours denote different years, and the bands show the 95% confidence intervals of the fitted double hyperbolic tangent function. The red dots indicate the fixed start and end days defined for the fitting.**

310 The estimated parameters describing different growing season phases, which were calculated from the fitted models, Eq. (2), show substantial differences between satellite and camera data (Table 4). At Halssiaapa and Kaamanen, the season start (SOS25) was estimated to start earlier based on the Sentinel-2 data, whereas at Lompolojänkkä the timing of SOS25 and MAX occurred later. The timing of the end of season (EOS25) was estimated later with the Sentinel-2 data at Halssiaapa and Kaamanen, while at Lompolojänkkä there was no systematic difference.



315 **Table 5: Growing season phases estimated from camera and satellite images (DOY): SOS25 (Start of season, 25% difference between start and maximum), MAX (maximum GCC) and EOS (End of season, 25% difference between end and maximum).**

Halssiaapa

	SOS25		Max			EOS25	
	Camera	Satellite	Camera	Satellite		Camera	Satellite
2015	157		2015	208		2015	257
2016	150	145	2016	197	222	2016	249 280
2017	170	157	2017	215	227	2017	251 258
2018	157	133	2018	212	191	2018	250 265
2019	152	139	2019	192	191	2019	265 288

Lompolojänkkä

	SOS25		Max			EOS25	
	Camera	Satellite	Camera	Satellite		Camera	Satellite
2015	157		2015	202		2015	258
2016	147	151	2016	193	211	2016	255 241
2017	168	167	2017	204	222	2017	264 265
2018	153	166	2018	196	208	2018	257 279
2019	149	152	2019	182	193	2019	274 273

Kaamanen

	SOS25		Max			EOS25	
	Camera	Satellite	Camera	Satellite		Camera	Satellite
2015	153		2015	213		2015	255
2016	147	139	2016	198	210	2016	250 258
2017	166	160	2017	211	222	2017	255 258
2018	149	139	2018	207	209	2018	253 288
2019	151	140	2019	201	195	2019	261 288

4 Discussion

320 In this study, we examined how phenology, described with GCC, varied in three natural peatlands in northern Finland during five growing seasons and how it depends on the site-specific characteristics and the composition of vegetation. The collected data allowed us to create a continuous representation of the development of greenness, which could be related to observed changes in the ecosystem-atmosphere flux of CO₂ and compared with the corresponding satellite-derived data.

325 We found the highest GCC values at Lompolojänkkä, a fen with high nutrient availability, rich vegetation and the highest LAI of the study sites (Fig. 4). The highest GCC also coincided with the highest photosynthetic productivity at peak summer. At Lompolojänkkä, the surface is flatter than at the other sites, where pronounced microtopography results in a higher variability in the hydrological features and consequently in the trophic status and vegetation. Also, the stream running through the Lompolojänkkä fen feeds water and nutrients to its surroundings (Lohila et al. 2010, Aurela et al. 2009). This affects fen's nutrient status and is reflected in vegetation, which mainly consists of annuals such as *Carex* spp. and *Menyanthes trifoliata*, and thus in
 330 the GCC and GPP_{max} reported here.



335 Related to the microtopographical differences between the study sites, we found a higher GCC in those plant community types that had annuals with bigger leaves and, correspondingly, a lower GCC in areas dominated by shrubs and mosses (Table 3, Appendices Fig. A1). The different plant communities also have different habitats. For example, shrubs thriving in drier locations such as strings, while many annuals (sedges, big-leaved bogbean) favour wetter environment.

340 Compared to traditional and more laborious measurements of plant growth, the digital camera-based measurements produce automatically high-frequency data in an effortless way. Even though the variation among the sites was greater than the variation between the ROIs within one site, our results indicate that vegetation monitoring is feasible even at the plant community level. To our knowledge, different plant communities have not been defined and compared from digital camera images with this precision before, and we conclude that these GCC observations of the differentially developing vegetation types have a potential to help decomposing an integrated CO₂ flux observation into components allocated to these vegetation types.

345 A warm spring leads to an earlier growing season start. Nevertheless, even though the growing season start was late at the study sites in 2017, due to a cold spring and late snow melt, vegetation was capable of reaching the same maximum GCC level as in other years, at Lompolojännkä and Kaamanen even attaining the maximum GCC and GPP_{max} observed during the whole study period (Fig. 5). A review of Wipf and Rixen (2010) on arctic and alpine ecosystems concluded that a delayed snowmelt and thus a shorter growing season decreases the overall plant productivity of an ecosystem, but it also noted that the effect of snowmelt timing depends on the plant functional type; for example, the growth of forbs increases while the growth of grasses decreases when the snowmelt occurs later. The later phenological phases are most likely controlled by GDDS rather than the timing of the growing season start (Wipf, 2010). Furthermore, the phenology of those plant species which usually start developing earlier after the snowmelt, and the first phenological phases of all plant species, are more sensitive to changes in the snowmelt timing. Our results imply that the northern peatland vegetation is capable of starting the growth quickly after a cold spring and the vegetation can even increase gross primary production, if the conditions are favourable later during the growing season, as was the case in 2017. This was clearly observed in the magnitude and timing of the maximum GCC. The faster GCC increase and lower temperature sensitivity at Lompolojännkä than at the other sites are explained by the nutrient status of this fen.

360 As observed in several studies conducted in different ecosystems (forests, grasslands, crops, peatlands), GPP correlates strongly with the greenness index derived from digital camera images (Richardson et al., 2008; Migliavacca et al., 2011; Keenan et al., 2014; Peichl et al., 2015; Toomey et al., 2015; Linkosalmi et al., 2016; Knox et al., 2017; Järveoja et al., 2018; Peichl et al., 2018; Koebisch et al., 2019). Our results agree with these studies, showing highly similar seasonal cycles of GCC and GPP_{max} at open peatlands dominated by shrubs and deciduous plants. Essentially, both are controlled by the amount of green leaf area, which in turn is driven mainly by temperature and day length (Bauerle et al., 2012; Peichl et al., 2015; Koebisch et al., 2019). When temperature increases, the plant chemical reaction rates also increase, triggering photosynthesis (Bonan, 2015). According to our results, air temperature, expressed here as a degree day sum (Fig. 5), explained well the annual differences in the early phase of the growing season, which has also been previously observed for a more southern boreal peatland (Peichl et al. 2015). In the latter part of the growing season, the decreasing day length and temperatures strongly drive the gradual degradation of chlorophyll content, which eventually leads to downregulation of photosynthesis and further to leaf fall and winter dormancy (Larcher, 2003; Öquist and Huner, 2003; Bonan, 2015).

370



While the differences in the phenological courses during different years are well depicted by GCC, also the variation in the maximum greenness level among the years and sites may be assessed by the phenocamera-derived GCC. Lompolojänkkä showed during all the years significantly higher maximum GCC and GPP_{max} than the other sites (Figs. 7 & 8, Table 2). Also, the maximum GCC and GPP_{max} were found in the same year at all sites. In addition to the seasonal cycles, both GCC and GPP show distinct
375 periods of correlated short-term variation, which is mainly controlled by abiotic factors, such as temperature and solar radiation (Peichl et al., 2015). For example, the variation in GCC and GPP_{max} was highly similar during the first part of the growing seasons of 2016 and 2017 at Kaamanen (Appendices Fig. A9 c) and during the drought period in 2018 at Halssiaapa (Figs. 7 & 8, Appendices Fig. A6). At Lompolojänkkä, this widespread drought did not result in a decrease of the water table level, which was due to the local hydrological features, and the net CO_2 uptake even increased in contrast to other northern sites (Rinne et al., 2010).
380 At Kaamanen, however, the drought decreased the CO_2 sink, counterbalancing the gain due to the earlier growing season start in 2018 (Heiskanen et al., 2021). Our data show that the drought in 2018 and 2019 affected the CO_2 sink most at Halssiaapa (Fig. 8, Appendices Fig. A7). The greenness data, both from the Sentinel-2 satellite and repeat photography, are in good accord with these observations of CO_2 flux dynamics (Figs. 7 & 9). Despite the specific periods of correlation, our regression analysis indicates that most of the variation in GPP_{max} can be explained by the common seasonal cycle, rather than the short-term variations of GCC
385 (Table 4).

The fitting of a hyperbolic tangent function to GCC data to characterize the basic phenological cycle worked well when data availability was sufficient (Figs. 7 & 9). The effect of poor data coverage is especially evident in the Sentinel-2 data in the beginning and end of the growing season, and also when the camera data were limited, e.g. in the early growing season at Halssiaapa in 2018
390 and at Kaamanen in 2019. Such data losses obviously compromise the accurate timing of the phenological phases. We also found large differences between the camera- and satellite-derived growing season phases (Table 4), the fits to the Sentinel-2 data suggesting a longer growing season at Halssiaapa and Kaamanen. Nevertheless, the main phenological changes during the growing season were visible also in the satellite data. Vrieling et al. (2018) found large differences between the phenological parameters derived from the satellite-based NDVI and camera-based GCC time series, especially in the end of the growing season. The
395 differences could be explained by the non-photosynthetic vegetation mass, such as dead plant matter, stems and flowers, which in an angled view affects the visibility of the green plant mass in the image. Thus, Vrieling et al. (2018) suggested that camera observations taken at nadir, rather than from an angled view, could produce better correlation between satellite and camera data. Also, it should be noted that the satellite indices are estimated from surface reflectance, while the camera image analysis applies raw digital numbers that scale with the reflected radiance (Vrieling et al., 2018). Thus, the resulting GCC estimates can be expected
400 to differ between the techniques, as also shown by the present study.

Obviously, the temporal coverage of non-cloudy satellite data, typically including an image every 5 to 10 days, is limited compared to the high-frequency camera-based measurements. The satellite data were limited especially during 2016 and 2017, because at that time Sentinel-2 constellation (Sentinel-2A and Sentinel-2B) consisted only of Sentinel-2A. Since 2018, however, there have
405 been data available from two satellites. Overall, mapping the vegetation on these heterogeneous peatlands with remote sensing methods is challenging and the suitability of the methods depends on the peatland structure (Räsänen et al., 2019). By providing local, continuous data even on the plant community level, digital photography could be used for verification of remote sensing products and as supporting information for their interpretation, as well as for filling the gaps in the landscape level data (Filippa et al., 2018; Richardson et al., 2007; Richardson et al., 2009; Sonnentag et al., 2012).

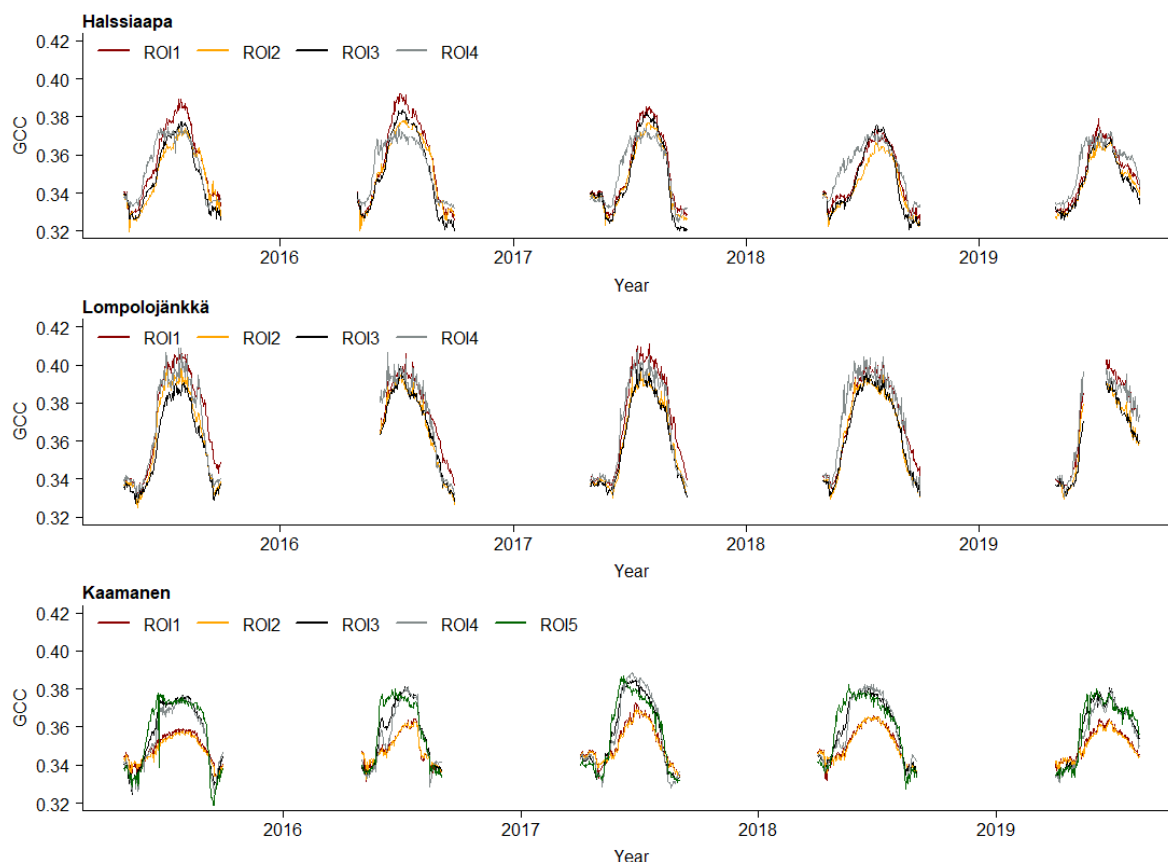


410 5 Conclusions

In this study, we showed that the digital photography derived greenness index (GCC) differed between three northern boreal peatland sites, being associated with nutrient availability and LAI. At all sites, the seasonal course of GCC was closely correlated with that of CO₂ uptake. The digital images also enabled determining the GCC of different plant communities, suggesting that these images can potentially be used for partitioning the ecosystem-scale CO₂ flux measurement. The spring temperatures and
415 consequent variation in growing season start affected GCC and GPP_{max}, but the peatland vegetation showed capability to compensate for a late start, and even to reach the maximum growth level observed during the five study years. The effect of drought on GCC and GPP_{max} depends on local hydrological features and thus the drought resistance of the site. Despite the seasonal coherence between the GCC and GPP_{max} data, the short-term variation of GCC did not in general explain the corresponding variation in GPP_{max}. The remote sensing (Sentinel-2) data were consistent with the camera-based results, but more satellite data
420 would be needed for a more reliable timing of different phenological phases. Finally, we conclude that the digital photography data could be used for verification, interpretation and gap filling of the remote sensing data.



Appendices



425 **Figure A1: The GCC of the different Region of Interests (ROIs) of specific plant communities. The numbers 1-5 indicate the different plant communities detailed in Table 1.**

430 **Table A1: The significant differences between different plant communities. The numbers 1-5 indicate the different plant communities detailed in Table 1. For interpretation, a denotes significant ($p < 0.05$) difference from ROI1, b denotes significant difference from ROI2, c denotes significant difference from ROI3, d denotes significant difference from ROI4 and e denotes significant difference from ROI5.**

	2015	2016	2017	2018	2019
Halssiaapa	ROI2 a ROI3 a, d	ROI3 a		ROI2 a ROI3 a, b, c	ROI2 a, d ROI3 a, d
Lompolojänkkä	ROI2 a, d ROI3 a, d	ROI2 a, d ROI3 a, d	ROI2 a, d ROI3 a, d	ROI2 a, d ROI3 a, d	ROI2 a, d ROI3 a, d
Kaamanen	ROI1 c, e ROI2 c, d, e	ROI1 c, e ROI2 c, e			ROI1 c, d, e ROI2 c, d, e

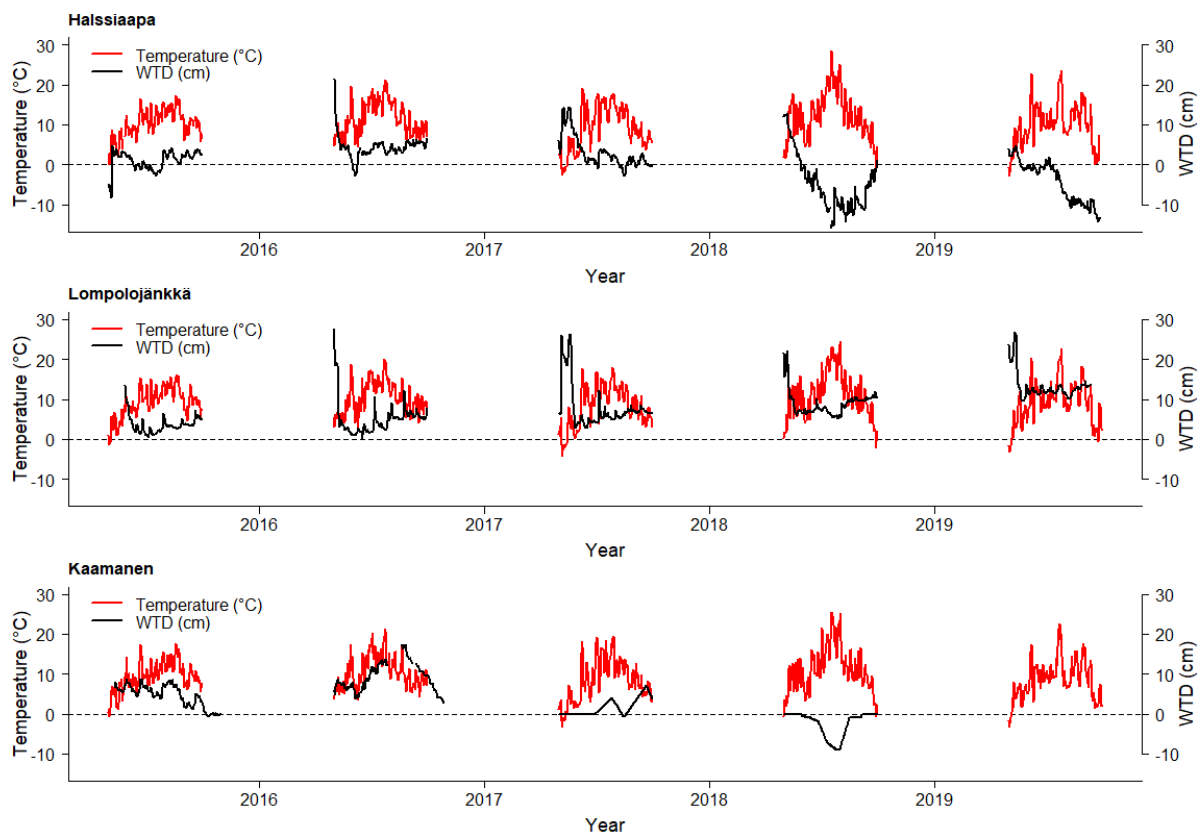
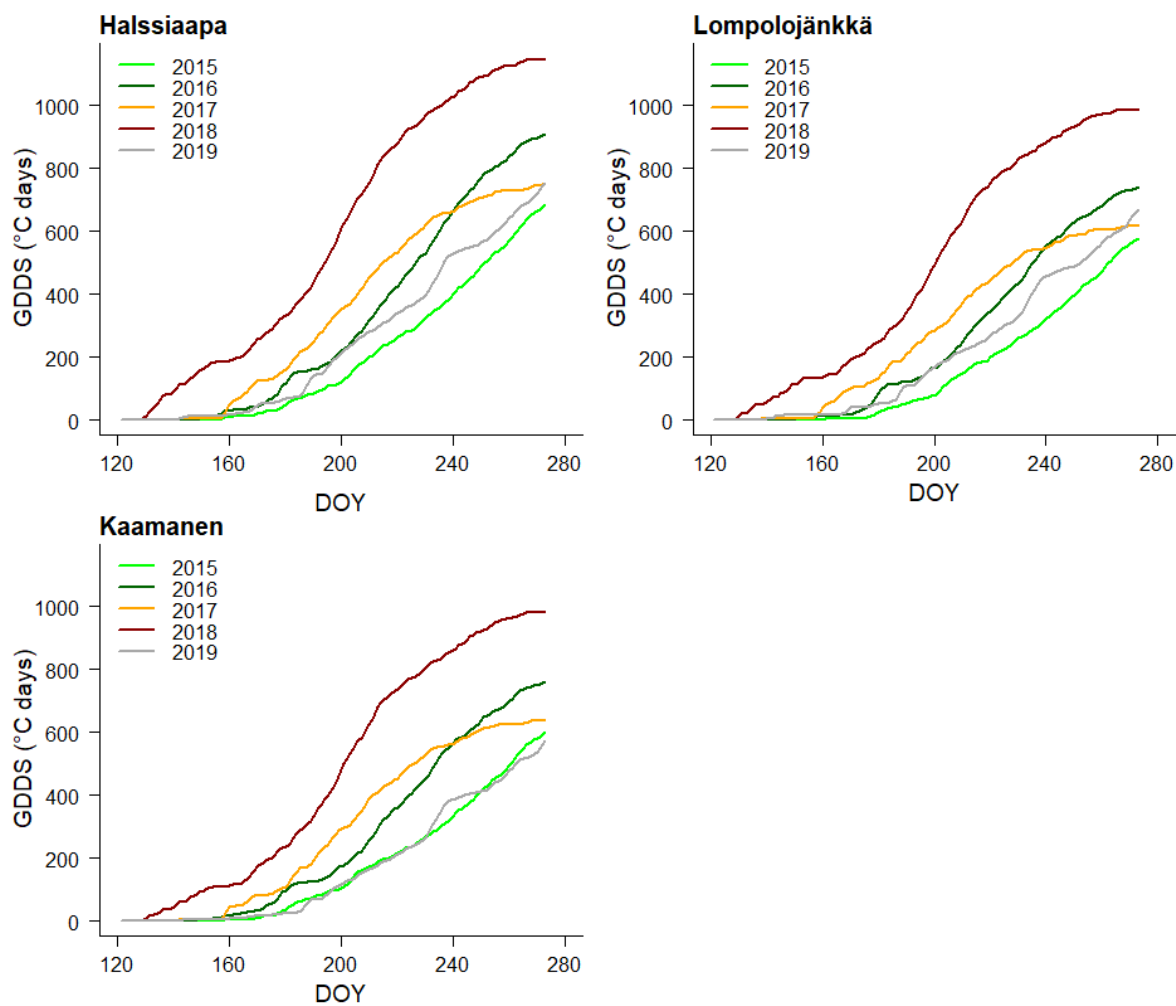


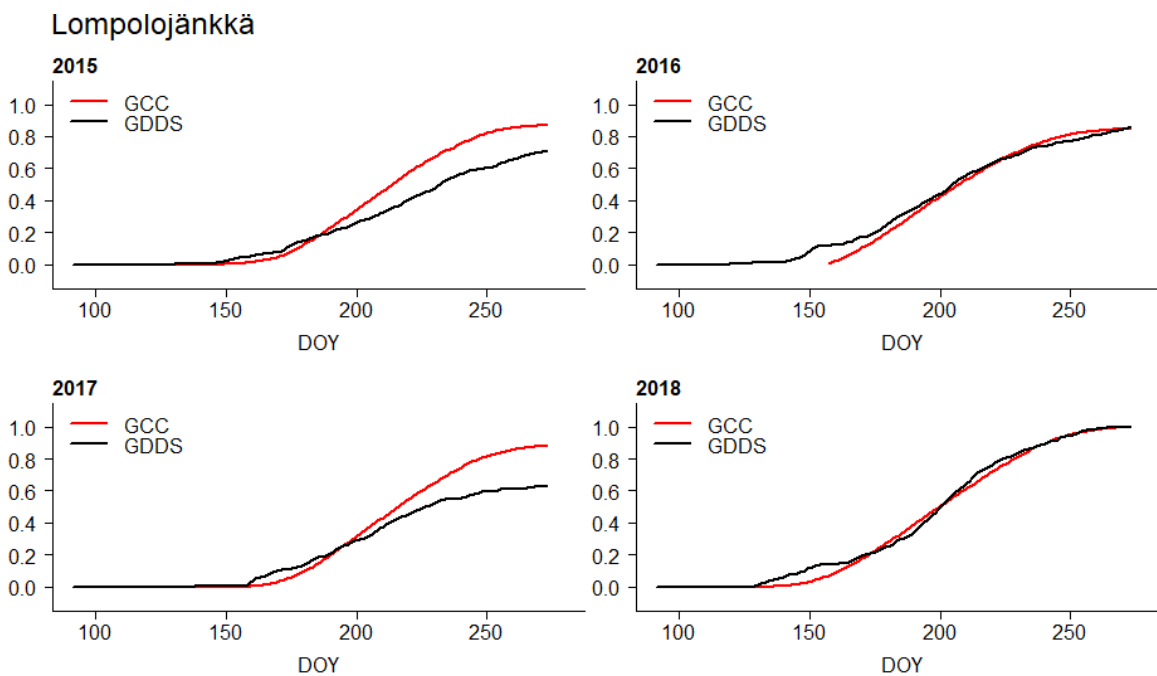
Figure A2: Daily mean temperatures (°C) and water table depths (cm) in 2015–2019 at the experimental sites.



435 Figure A3: The growing degree days (GDDs) in 2015 – 2019 at the experimental sites.



Figure A4 a: The normalized cumulative GCC and growing degree days (GDDS) in 2015 – 2019 at the experimental sites.



440 **Figure A4 b:** The normalized cumulative GCC and growing degree days (GDDs) in 2015 – 2019 at the experimental sites. The data from 2019 is missing.

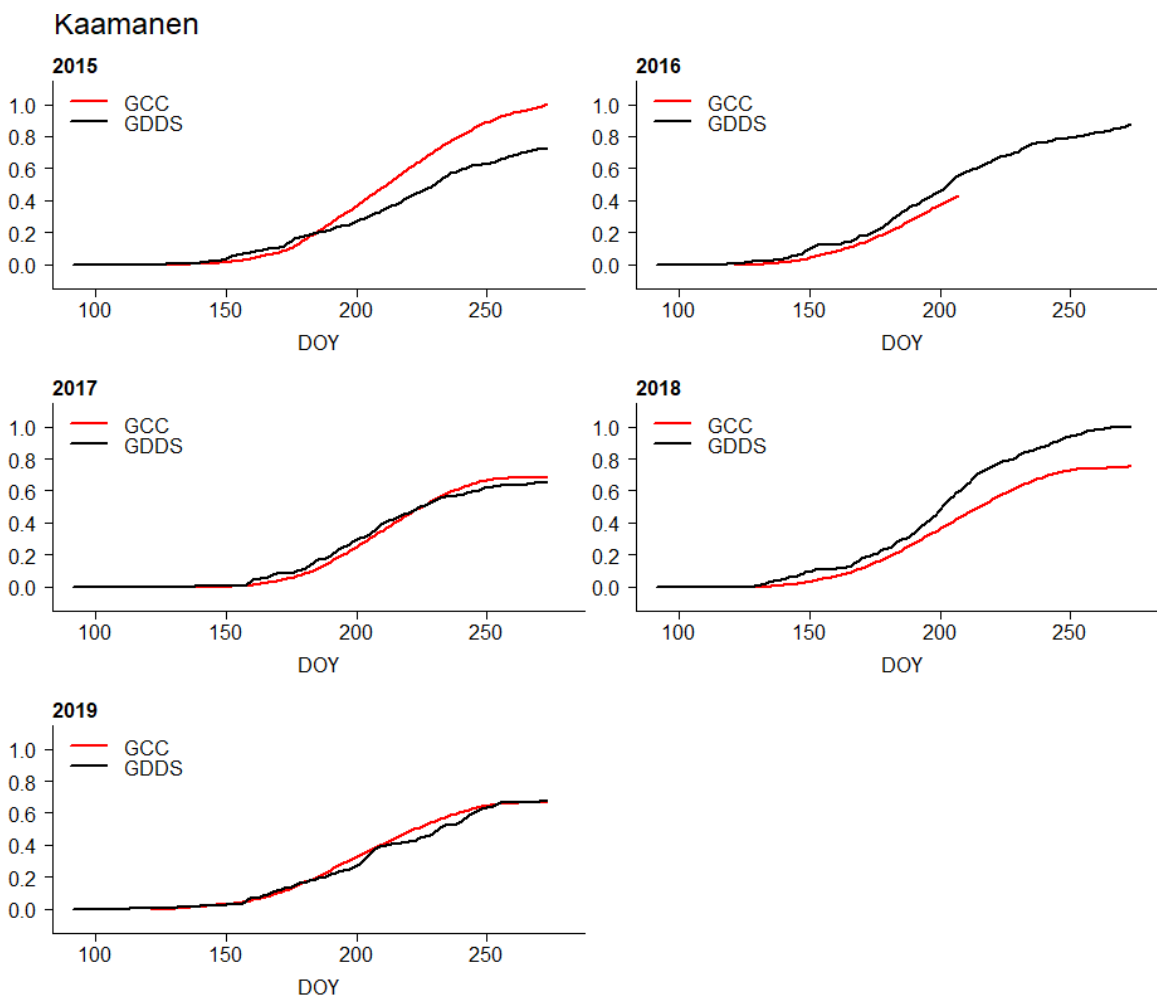
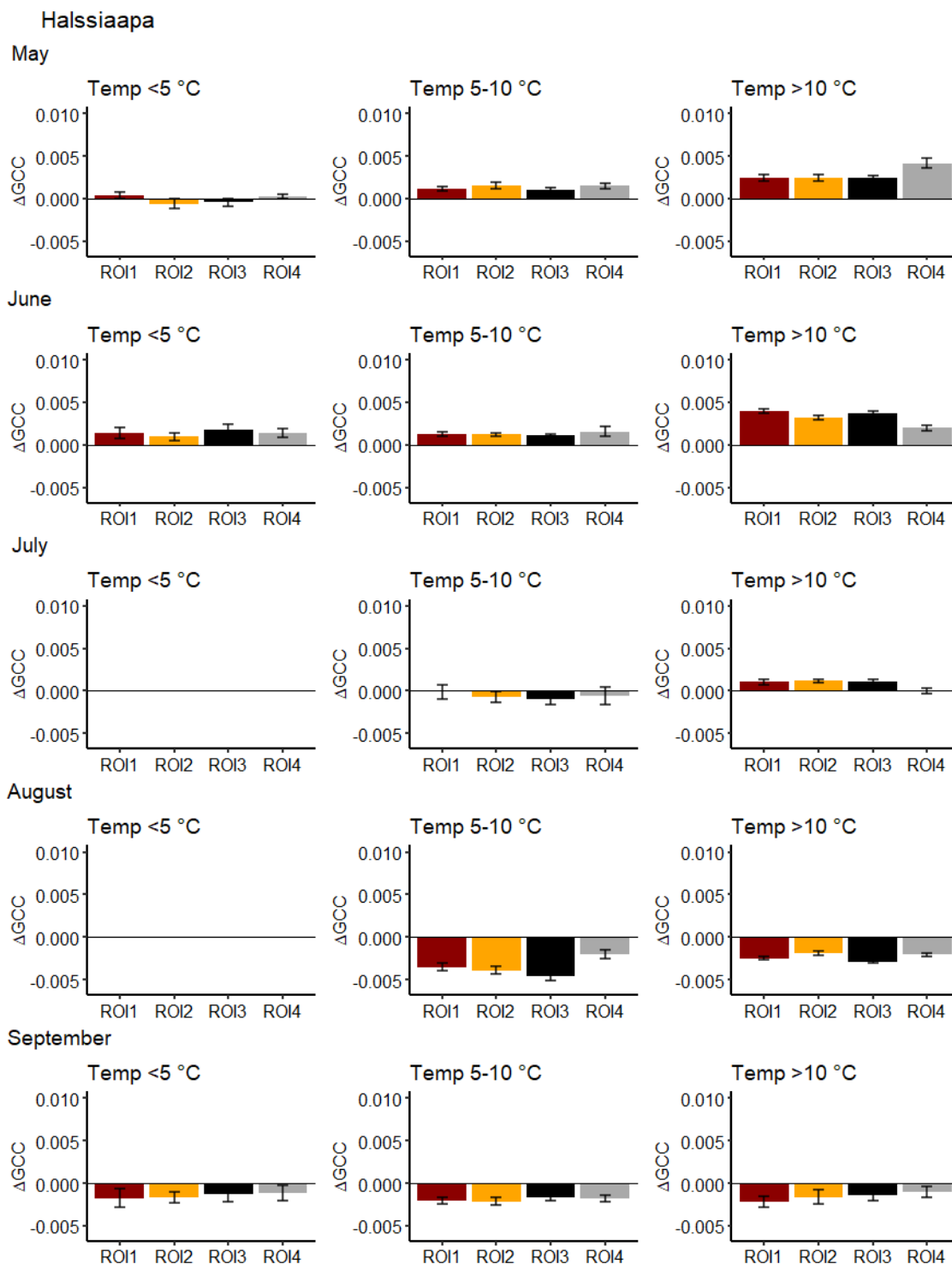


Figure A4 c: The normalized cumulative GCC and growing degree days (GDDS) in 2015 – 2019 at the experimental sites.



445 **Figure A5 a:** Mean three-day difference in GCC divided to temperature classes (<5 °C, 5-10 °C, >10 °C) at Halssiaapa from May to September. No temperature data in class <5 °C from July and August. The error bars denote the standard error.

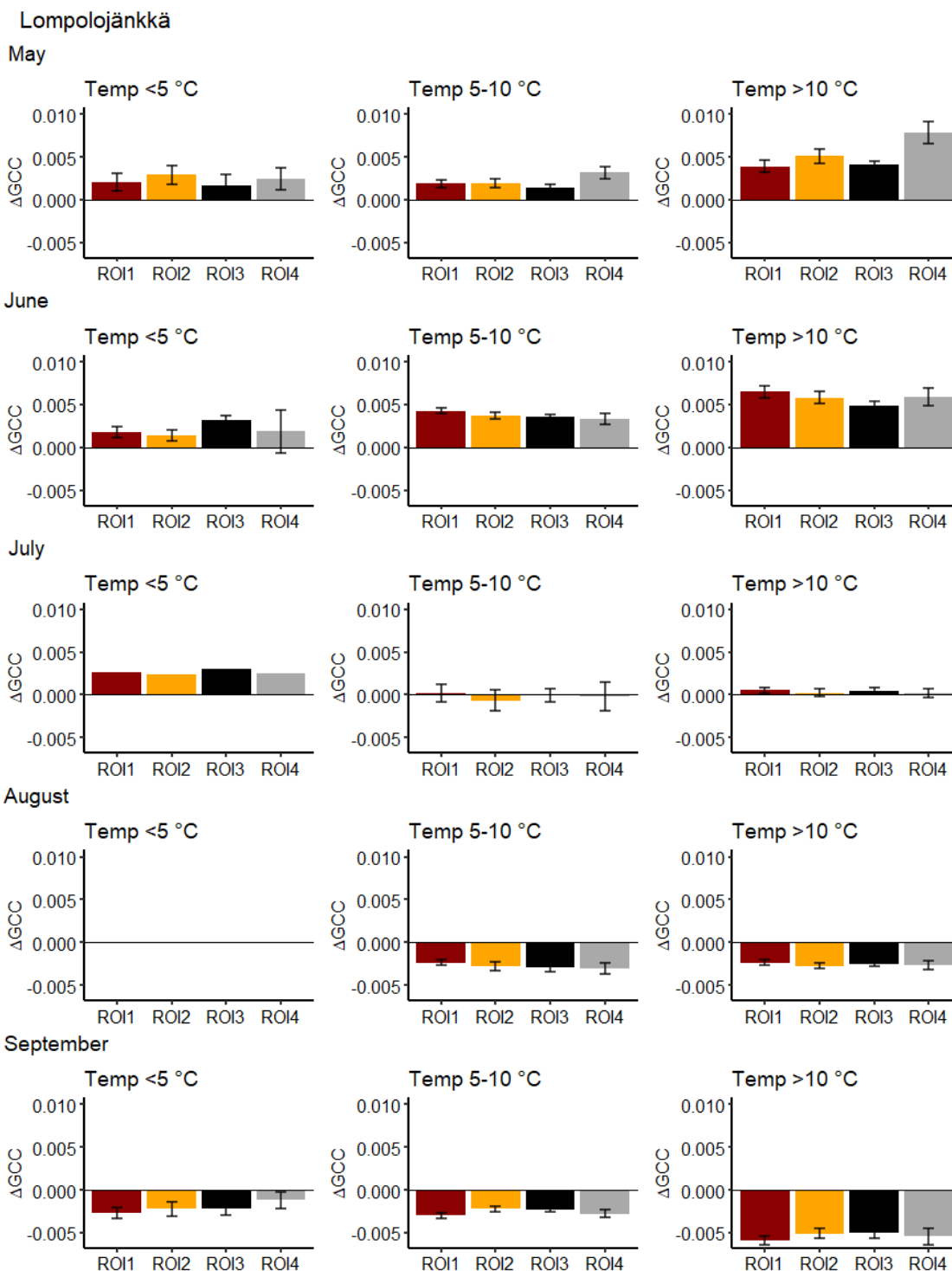
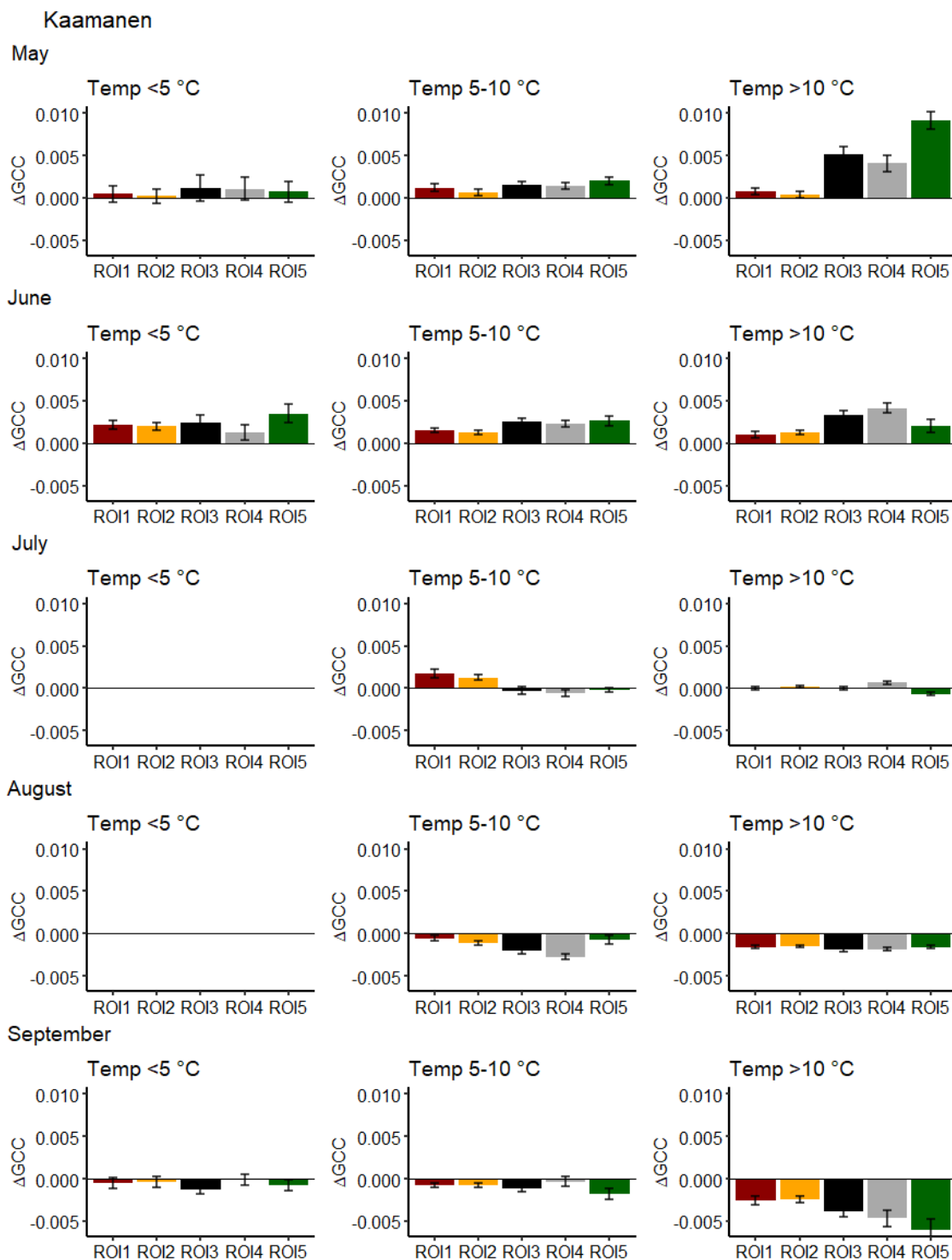
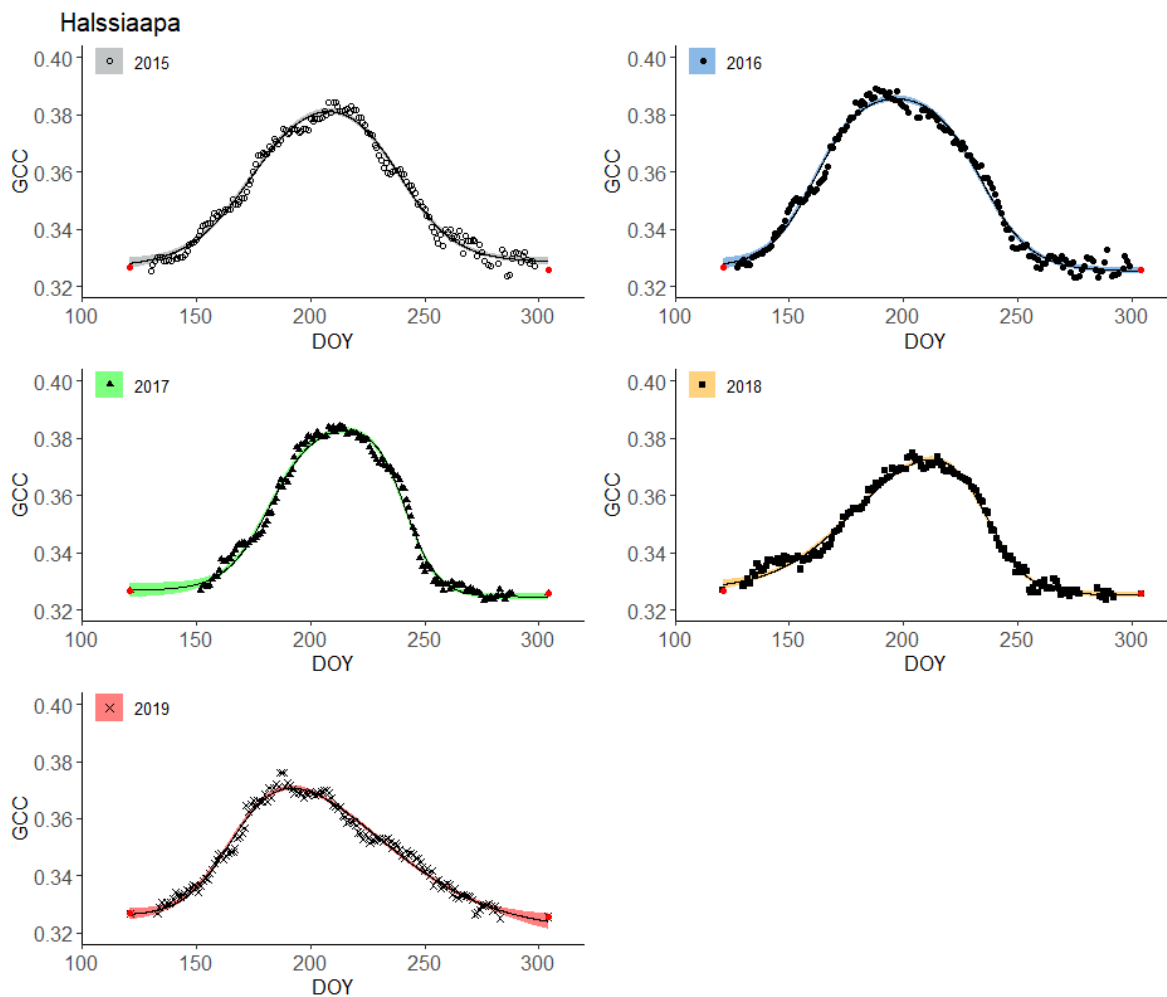


Figure A5 b: Mean three-day difference in GCC divided to temperature classes (<5 °C, 5-10 °C, >10 °C) at Lompolojänkkä from May to September. No temperature data in class <5 °C from July and August. The error bars denote the standard error.



450

Figure A5 c: Mean three-day difference in GCC divided to temperature classes ($<5\text{ }^{\circ}\text{C}$, $5\text{-}10\text{ }^{\circ}\text{C}$, $>10\text{ }^{\circ}\text{C}$) at Kaamanen from May to September. No temperature data in class $<5\text{ }^{\circ}\text{C}$ from July and August. The error bars denote the standard error.



455 **Figure A6 a:** The GCC values and fitted function with 95% confidence intervals in 2015 – 2019 at Halssiaapa. The red dots stand for the fixed start and end point of time in the fitting.

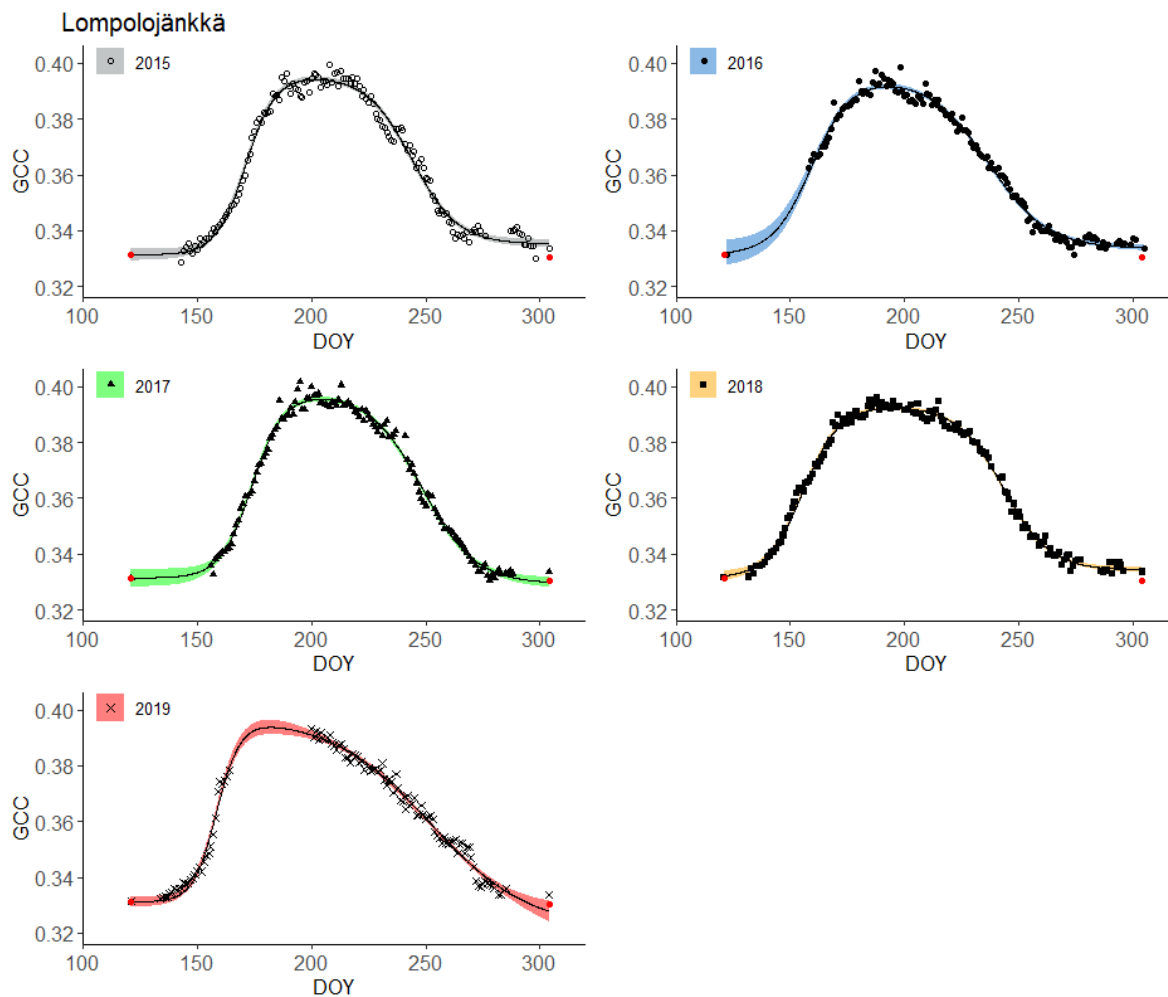
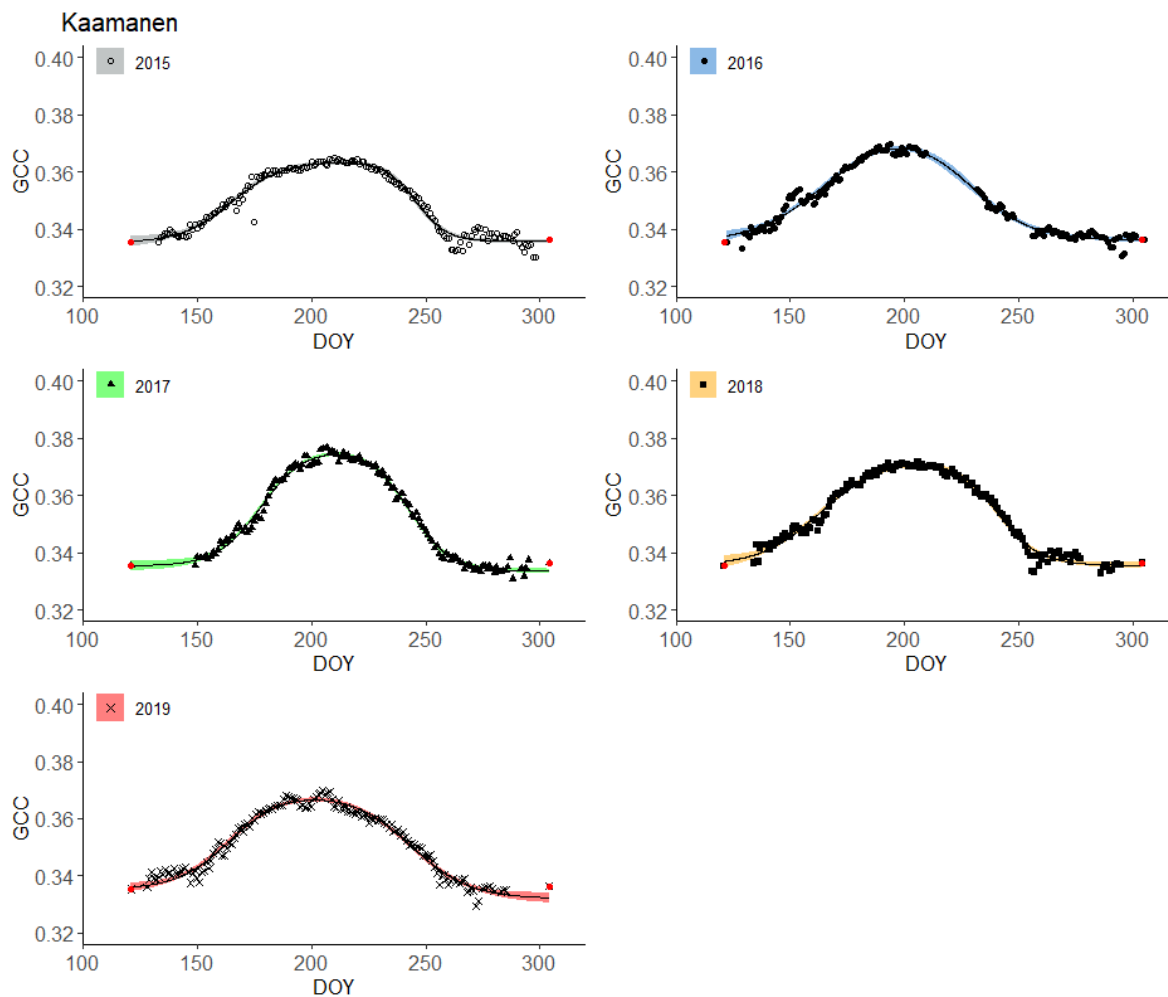


Figure A6 b: The GCC values and fitted function with 95% confidence intervals in 2015 – 2019 at Lompolojänkkä. The red dots stand for the fixed start and end point of time in the fitting.



460 **Figure A6 c:** The GCC values and fitted function with 95% confidence intervals in 2015 – 2019 at Kaamanen. The red dots stand for the fixed start and end point of time in the fitting.

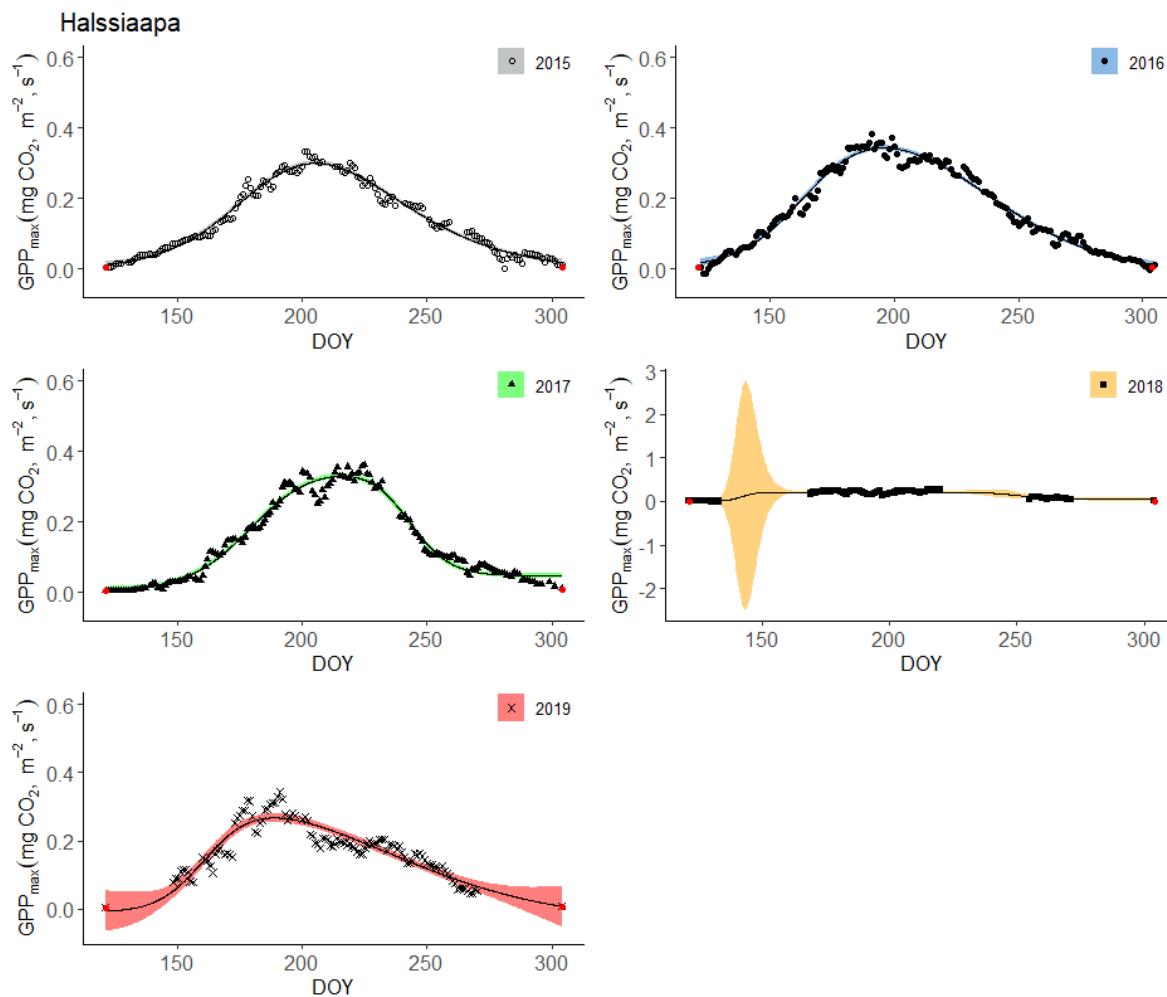
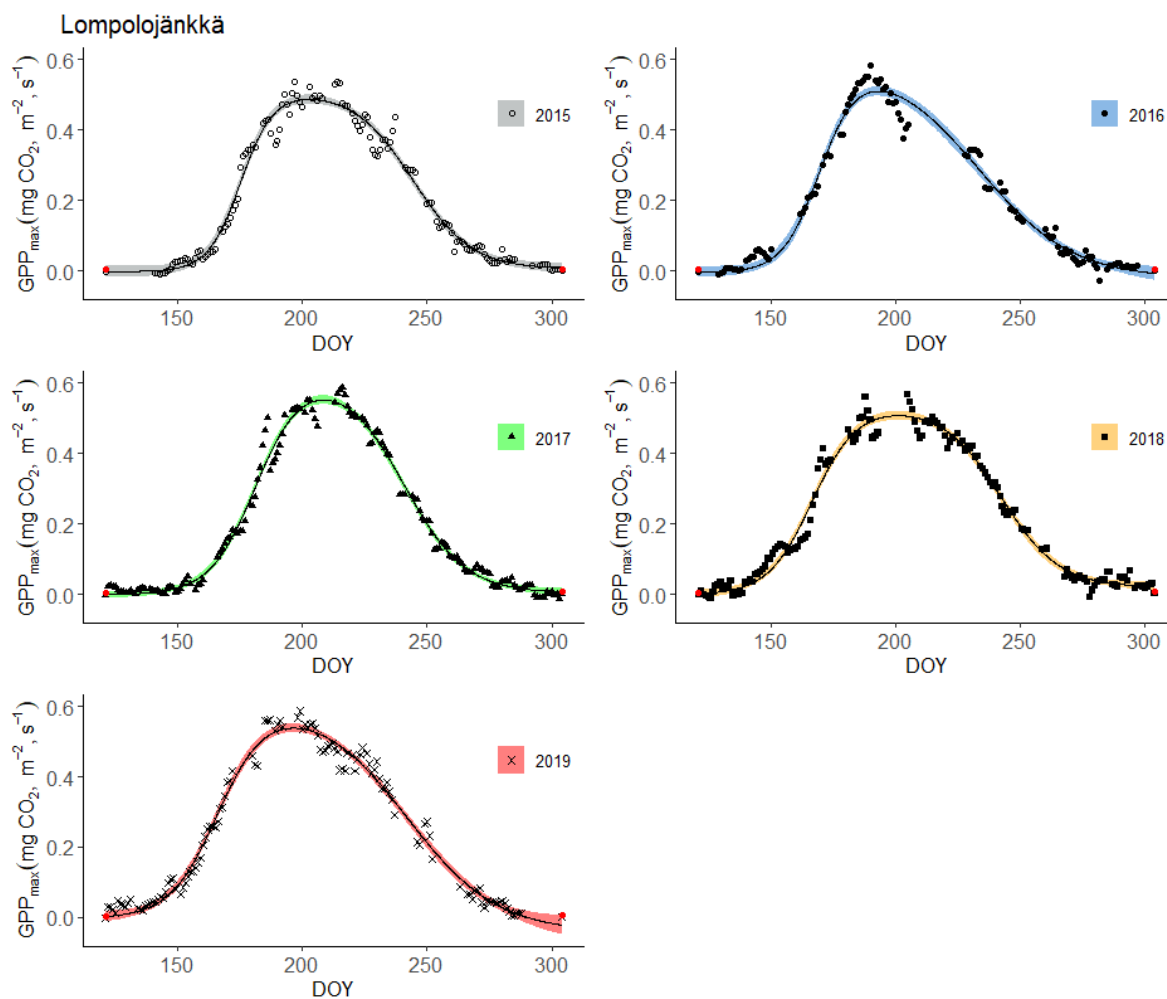
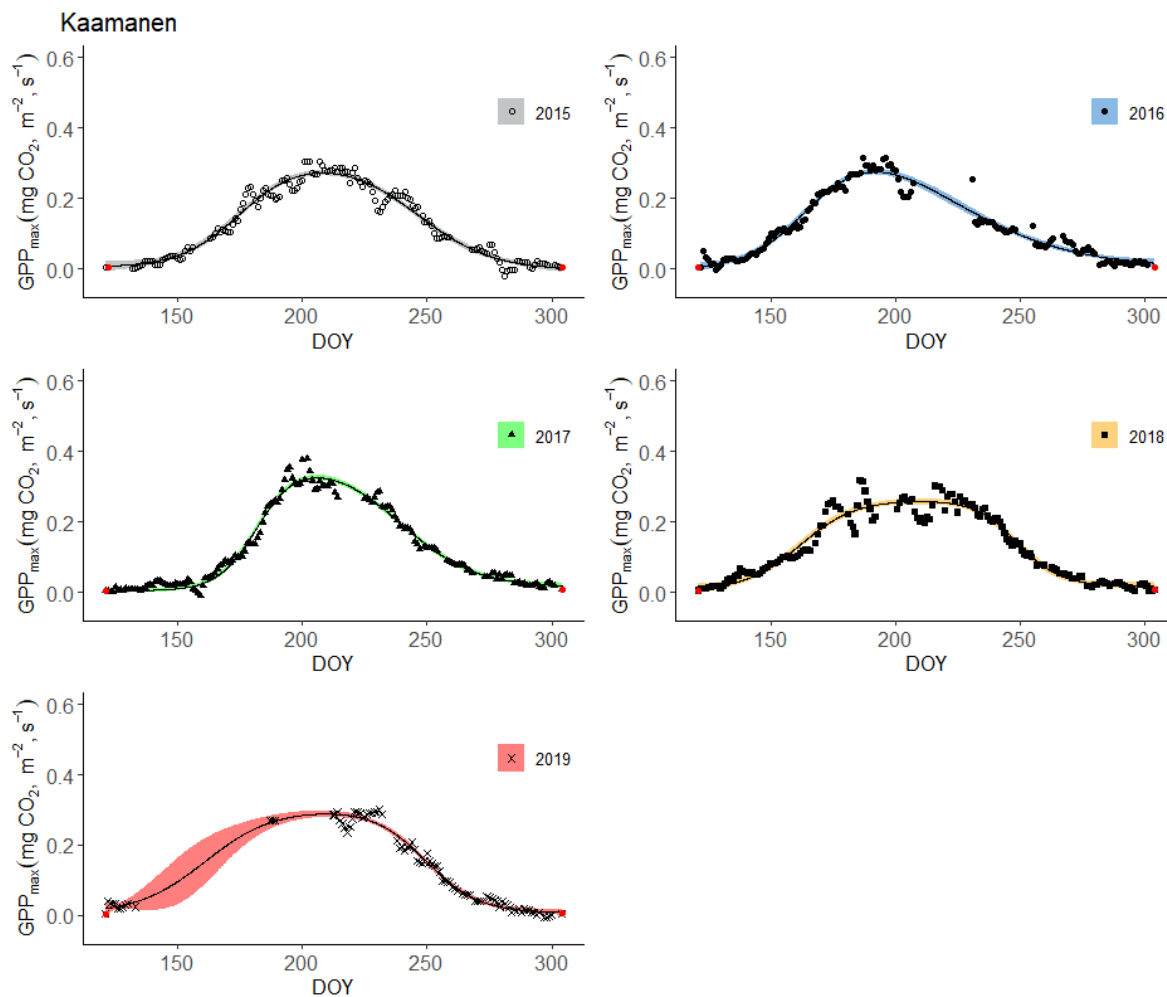


Figure A7 a: The GPPmax values and fitted function with 95% confidence intervals in 2015 – 2019 at Halssiaapa. Note the different scale in 2018. The red dots stand for the fixed start and end point of time in the fitting.



465

Figure A7 b: The GPP_{max} values and fitted function with 95% confidence intervals in 2015 – 2019 at Lompolojänkkä. The red dots stand for the fixed start and end point of time in the fitting.



470 **Figure A7 c:** The GPP_{max} values and fitted function with 95% confidence intervals in 2015 – 2019 at Kaamanen. The red dots stand for the fixed start and end point of time in the fitting.

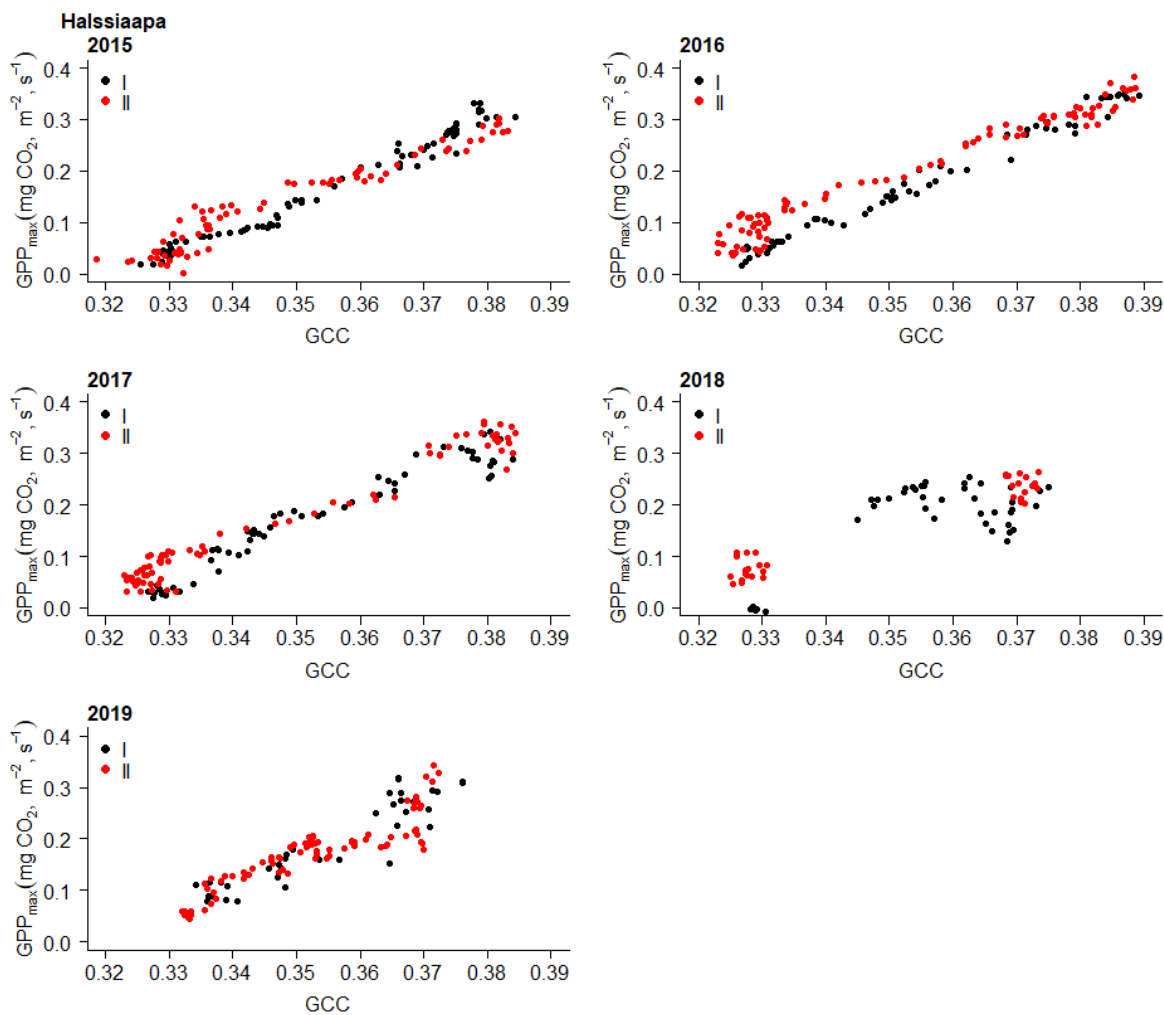
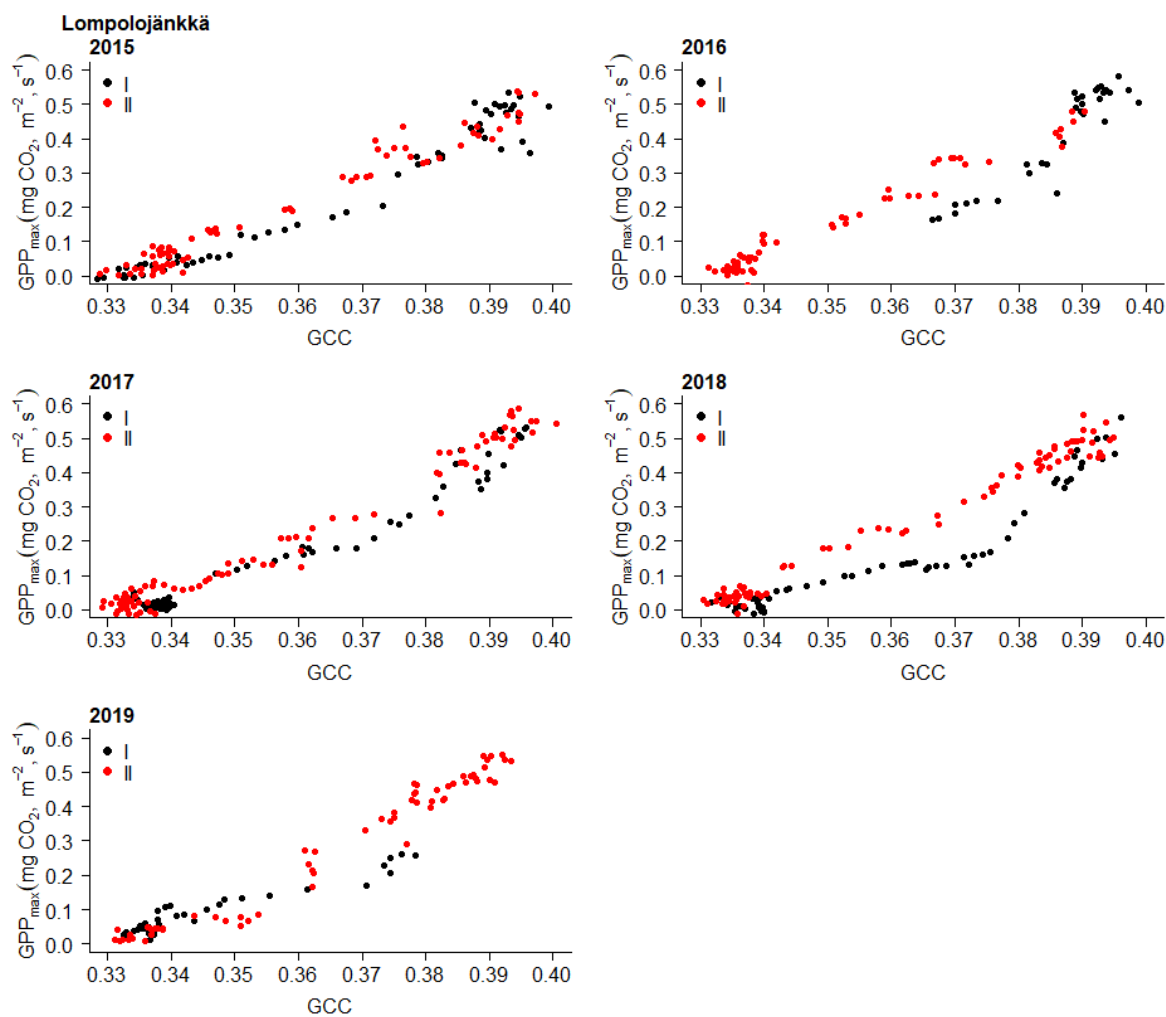


Figure A8 a: The regression between GCC and GPPmax at Halssiaapa in 2015–2019. The first part of the growing season is denoted with black circles, the latter half with red circles.



475 **Figure A8 b:** The regression between GCC and GPPmax at Lompolojänkkä in 2015–2019. The first part of the growing season is denoted with black circles, the latter half with red circles.

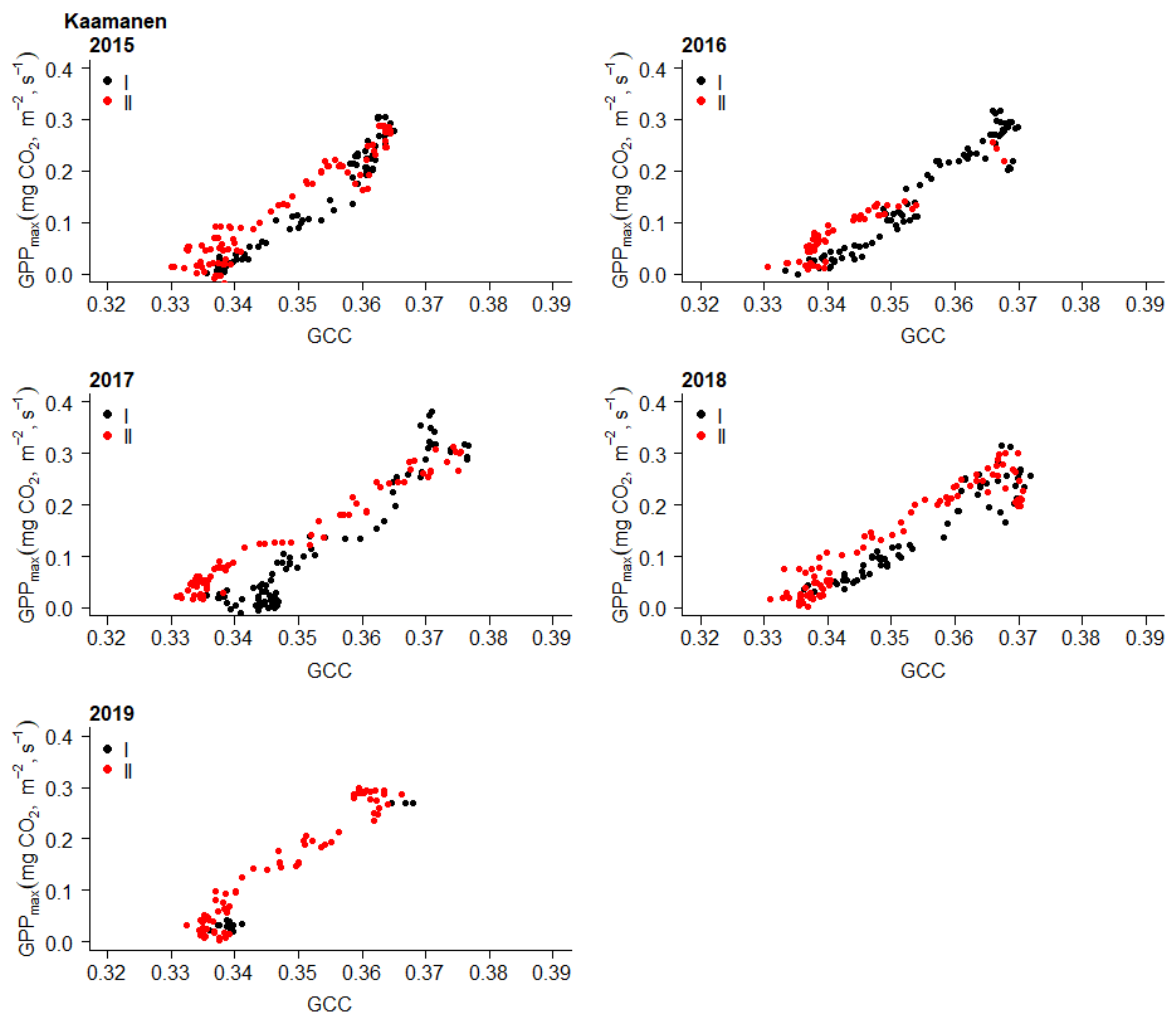
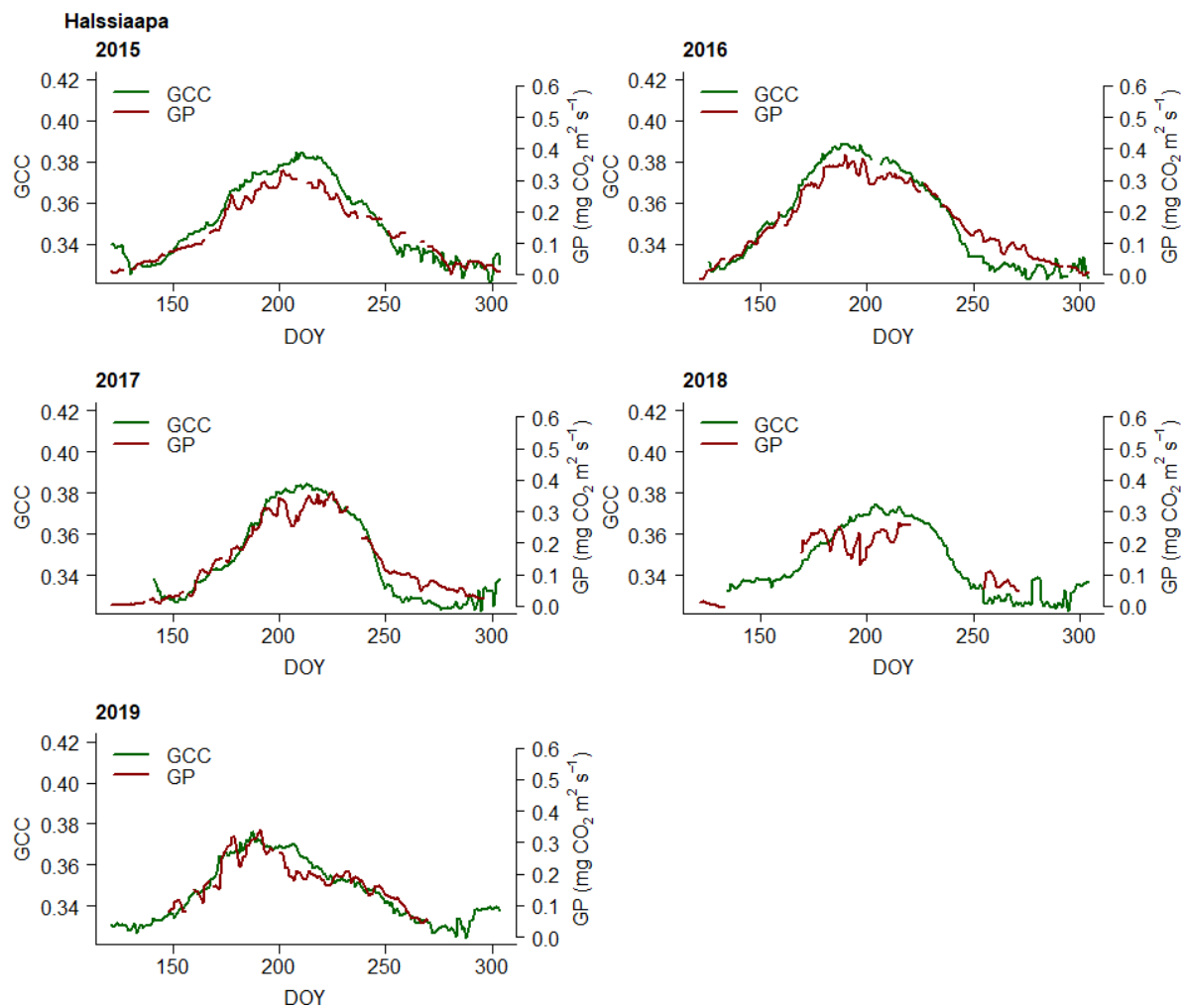


Figure A8 c: The regression between GCC and GPPmax at Kaamanen in 2015–2019. The first part of the growing season is denoted with black circles, the latter half with red circles.



480

Figure A9 a: The scaled GCC and GPPmax data at Halssiaapa in 2015–2019.

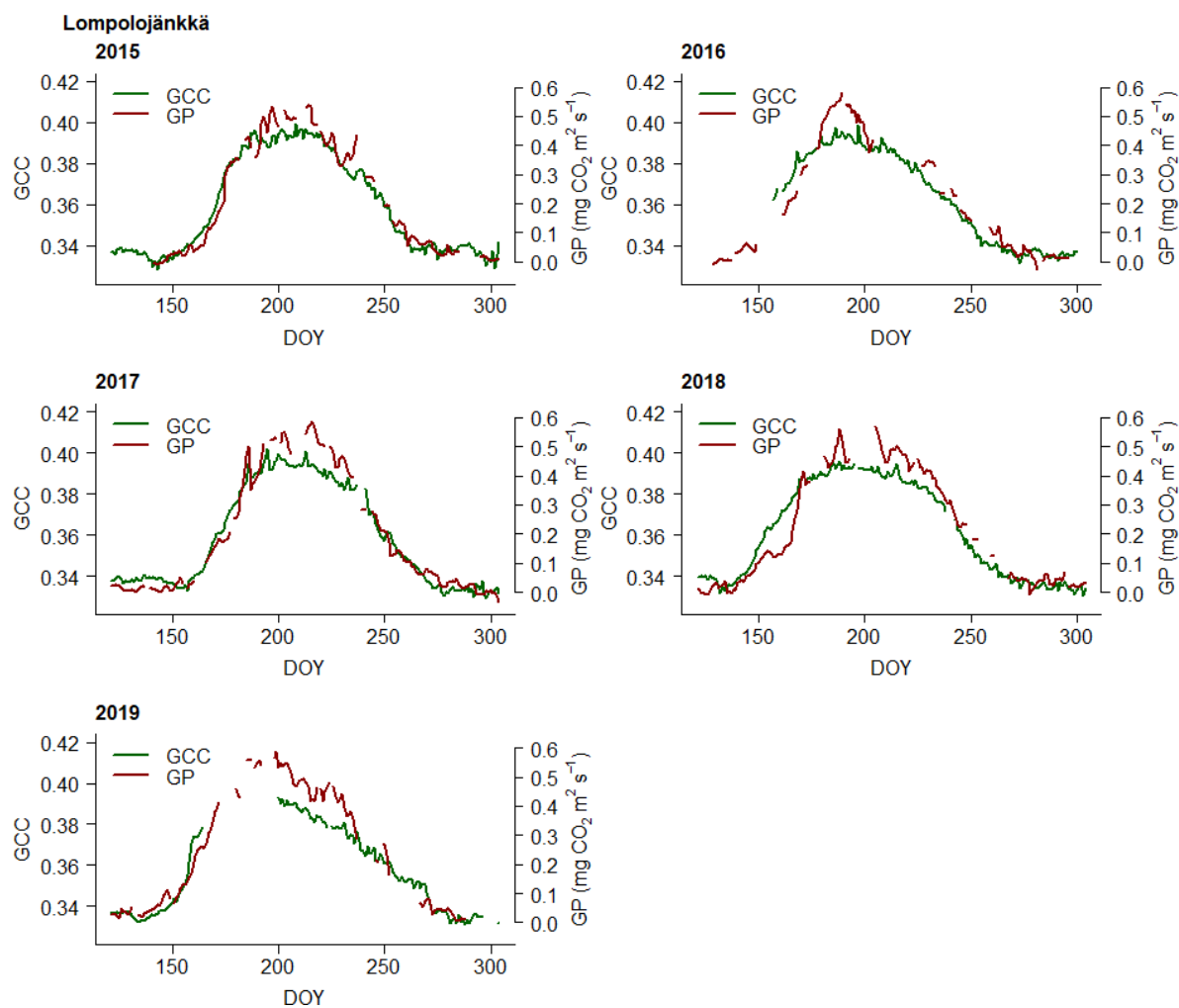
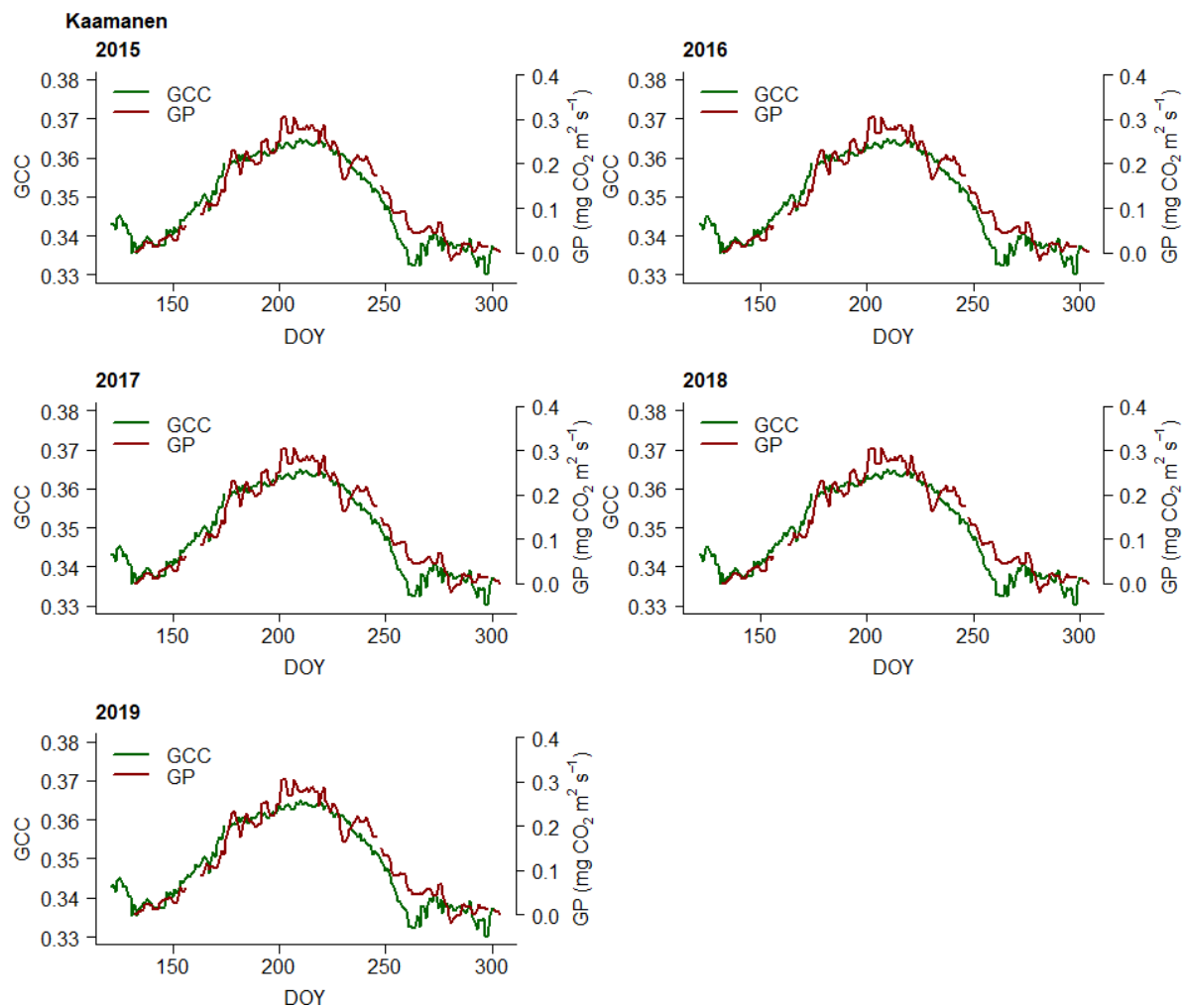


Figure A9 b: The scaled GCC and GPPmax data at Lompolojänkkä in 2015–2019.



485 Figure A9 c: The scaled GCC and GPPmax data at Kaamanen in 2015–2019.

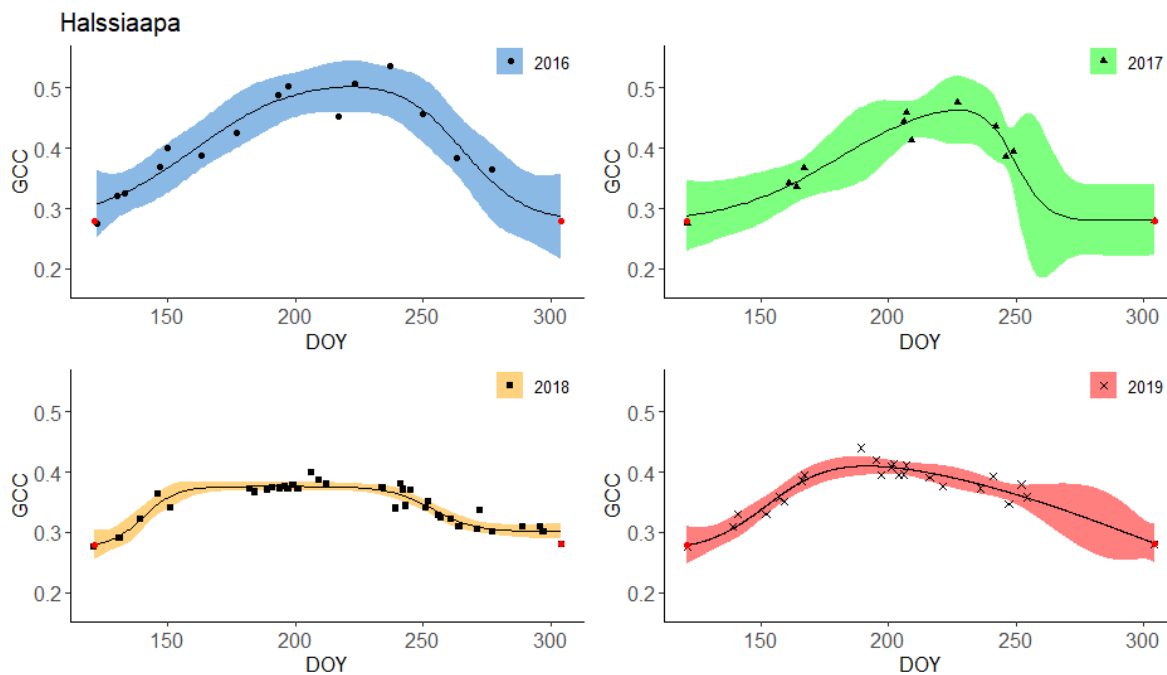
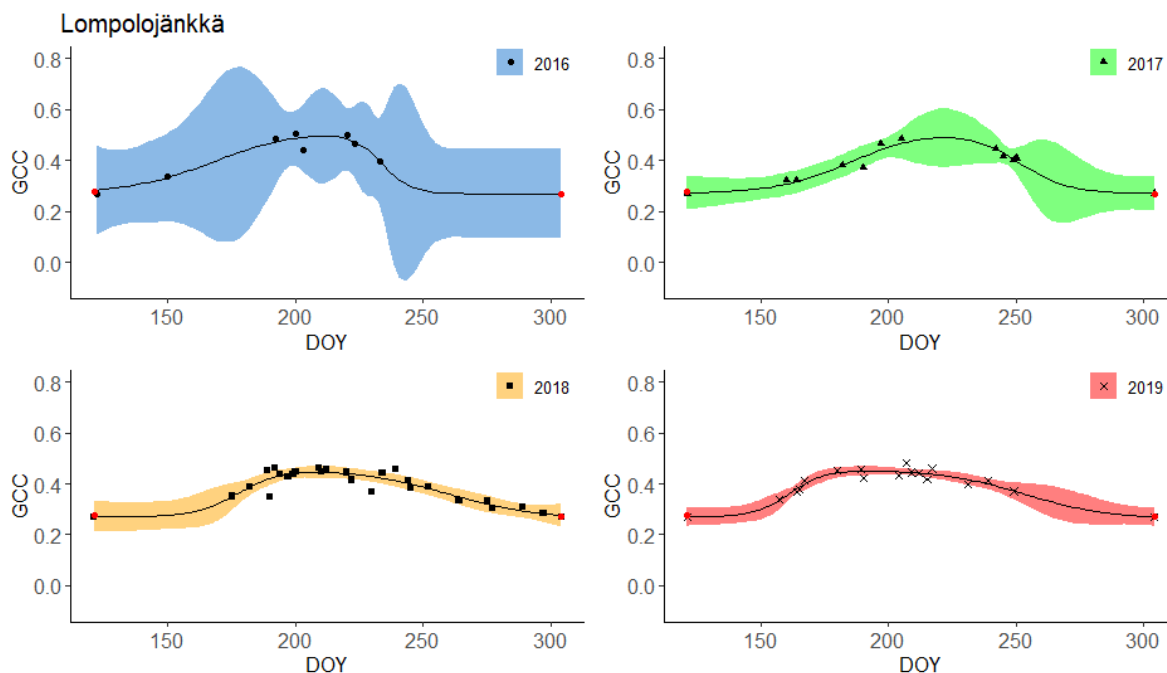


Figure A10 a: The Sentinel-2 derived GCC values and fitted function with 95% confidence intervals in 2016 – 2019 at Halssiaapa. The red dots stand for the fixed start and end point of time in the fitting.



490 Figure A10 b: The Sentinel-2 derived GCC values and fitted function with 95% confidence intervals in 2016 – 2019 at Lompolojänkkä. The red dots stand for the fixed start and end point of time in the fitting.

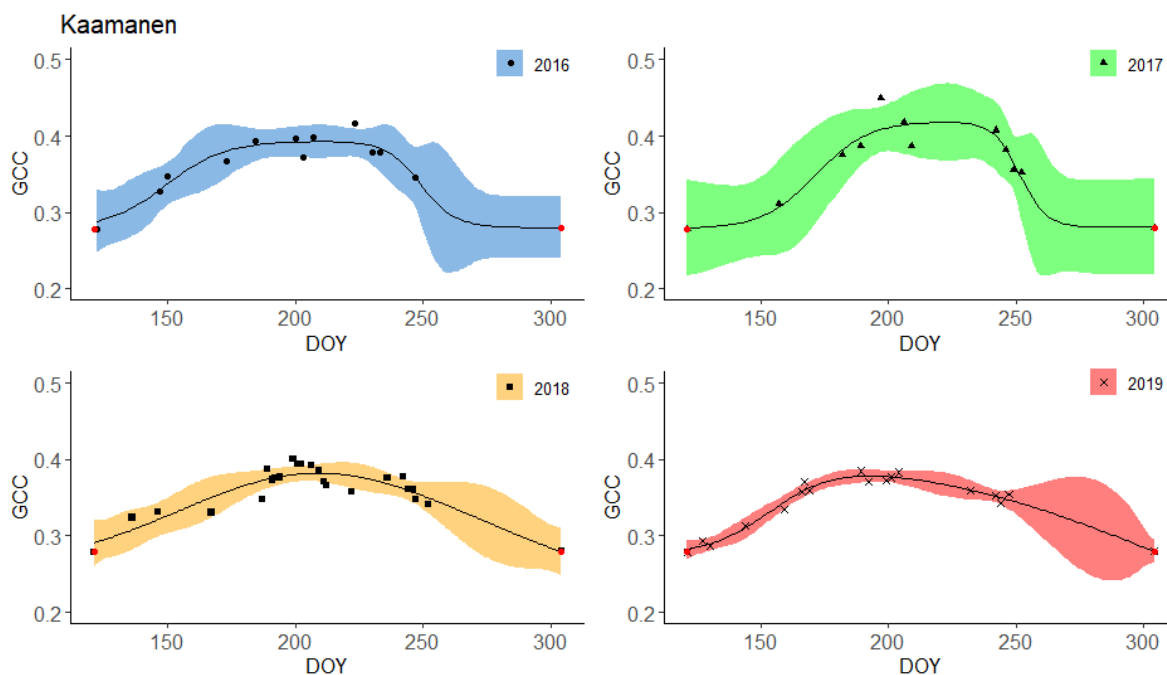


Figure A10 c: The Sentinel-2 derived GCC values and fitted function with 95% confidence intervals in 2016 – 2019 at Kaamanen. The red dots stand for the fixed start and end point of time in the fitting.

495 Author contribution

ANA, MP and TL were responsible for enabling and establishing the camera network. MA, ML and JR were part of executing the digital camera setup. MA and AL provided CO₂ measurements and environmental variables. MA and J-PT were responsible for post-processing the CO₂ data. ON performed the satellite (Sentinel-2) data analysis. CMT developed the image processing tool (FMIPROT). ML performed the digital camera image analysis and drafted the manuscript. MA, ML and J-PT contributed to the interpretation of results and writing on the first version of the manuscript. All authors commented on the manuscript.

Competing interests

The authors declare that they have no conflict of interest.

Acknowledgements

This research has been supported by the Academy of Finland (CAPTURE, grant no. 296888) and the EU (MONIMET Project (LIFE12ENV/FI/000409) funded by EU Life+ Programme 2013–2017).



References

- Ahrends, H. E., Etzold, S., Kutsch, W. L., Stoeckli, R., Bruegger, R., Jeanneret, F., Wanner, H., Buchmann, N., and Eugster, W.: Tree phenology and carbon dioxide fluxes: use of digital photography for process-based interpretation at the ecosystem scale, 39, 261–274, <https://doi.org/10.3354/cr00811>, 2009.
- 510 Aurela, M., Tuovinen, J.-P., and Laurila, T.: Carbon dioxide exchange in a subarctic peatland ecosystem in northern Europe measured by the eddy covariance technique, *Journal of Geophysical Research: Atmospheres*, 103, 11289–11301, <https://doi.org/10.1029/98JD00481>, 1998.
- Aurela, M., Tuovinen, J.-P., and Laurila, T.: Net CO₂ exchange of subarctic mountain birch ecosystem, 70, 135–148, <https://doi.org/10.1007/s007040170011>, 2001.
- 515 Aurela, M., Lohila, A., Tuovinen, J.-P., Hatakka, J., Riutta, T., and Laurila, T.: Carbon dioxide exchange on a northern boreal fen, 14, 699–710, 2009.
- Barr, A. G., Black, T. A., Hogg, E. H., GRIFFIS, T. J., Morgenstern, K., Kljun, N., Theede, A., and Nescic, Z.: Climatic controls on the carbon and water balances of a boreal aspen forest, 1994–2003, *Global Change Biology*, 13, 561–576, <https://doi.org/10.1111/j.1365-2486.2006.01220.x>, 2007.
- 520 Bauerle, W. L., Oren, R., Way, D. A., Qian, S. S., Stoy, P. C., Thornton, P. E., Bowden, J. D., Hoffman, F. M., and Reynolds, R. F.: Photoperiodic regulation of the seasonal pattern of photosynthetic capacity and the implications for carbon cycling, *Proc Natl Acad Sci USA*, 109, 8612, <https://doi.org/10.1073/pnas.1119131109>, 2012.
- Berninger, F.: Effects of Drought and Phenology on GPP in *Pinus sylvestris*: A Simulation Study Along a Geographical Gradient, 11, 33–42, 1997.
- 525 Black, T. A., Chen, W. J., Barr, A. G., Arain, M. A., Chen, Z., Nescic, Z., Hogg, E. H., Neumann, H. H., and Yang, P. C.: Increased carbon sequestration by a boreal deciduous forest in years with a warm spring, *Geophysical Research Letters*, 27, 1271–1274, <https://doi.org/10.1029/1999GL011234>, 2000.
- Bonan, G.: *Ecological Climatology: Concepts and Applications*, 3rd ed., Cambridge University Press, Cambridge, <https://doi.org/10.1017/CBO9781107339200>, 2015.
- 530 Bryant, R. G. and Baird, A. J.: The spectral behaviour of Sphagnum canopies under varying hydrological conditions, *Geophysical Research Letters*, 30, <https://doi.org/10.1029/2002GL016053>, 2003.
- Delbart, N., Picard, G., Le Toan, T., Kergoat, L., Quegan, S., Woodward, I., Dye, D., and Fedotova, V.: Spring phenology in boreal Eurasia over a nearly century time scale, *Global Change Biology*, 14, 603–614, <https://doi.org/10.1111/j.1365-2486.2007.01505.x>, 2008.
- 535 Dunn, A. L., Barford, C. C., Wofsy, S. C., Goulden, M. L., and Daube, B. C.: A long-term record of carbon exchange in a boreal black spruce forest: means, responses to interannual variability, and decadal trends, *Global Change Biology*, 13, 577–590, <https://doi.org/10.1111/j.1365-2486.2006.01221.x>, 2007.
- Filippa, G., Cremonese, E., Migliavacca, M., Galvagno, M., Sonnentag, O., Humphreys, E., Hufkens, K., Ryu, Y., Verfaillie, J., Morra di Cella, U., and Richardson, A. D.: NDVI derived from near-infrared-enabled digital cameras: Applicability across different plant functional types, *Agricultural and Forest Meteorology*, 249, 275–285, <https://doi.org/10.1016/j.agrformet.2017.11.003>, 2018.
- 540 Gorham, E.: Northern Peatlands: Role in the Carbon Cycle and Probable Responses to Climatic Warming, *Ecological Applications*, 1, 182–195, <https://doi.org/10.2307/1941811>, 1991.
- Goulden, M. L., Munger, J. W., Fan, S.-M., Daube, B. C., and Wofsy, S. C.: Measurements of carbon sequestration by long-term eddy covariance: methods and a critical evaluation of accuracy, *Global Change Biology*, 2, 169–182, <https://doi.org/10.1111/j.1365-2486.1996.tb00070.x>, 1996.
- 545 Heiskanen, L., Tuovinen, J.-P., Räsänen, A., Virtanen, T., Juutinen, S., Lohila, A., Penttilä, T., Linkosalmi, M., Mikola, J., Laurila, T., and Aurela, M.: Carbon dioxide and methane exchange of a patterned subarctic fen during two contrasting growing seasons, 18, 873–896, <https://doi.org/10.5194/bg-18-873-2021>, 2021.
- Ide, R. and Oguma, H.: Use of digital cameras for phenological observations, *Ecological Informatics*, 5, 339–347, <https://doi.org/10.1016/j.ecoinf.2010.07.002>, 2010.



- Järveoja, J., Nilsson, M. B., Gažovič, M., Crill, P. M., and Peichl, M.: Partitioning of the net CO₂ exchange using an automated chamber system reveals plant phenology as key control of production and respiration fluxes in a boreal peatland, *Global Change Biology*, 24, 3436–3451, <https://doi.org/10.1111/gcb.14292>, 2018.
- 555 Keeling, C. D., Chin, J. F. S., and Whorf, T. P.: Increased activity of northern vegetation inferred from atmospheric CO₂ measurements, *Nature*, 382, 146–149, <https://doi.org/10.1038/382146a0>, 1996.
- Keenan, T. F., Gray, J., Friedl, M. A., Toomey, M., Bohrer, G., Hollinger, D. Y., Munger, J. W., O’Keefe, J., Schmid, H. P., Wing, I. S., Yang, B., and Richardson, A. D.: Net carbon uptake has increased through warming-induced changes in temperate forest phenology, *Nature Climate Change*, 4, 598–604, <https://doi.org/10.1038/nclimate2253>, 2014.
- 560 Knox, S. H., Dronova, I., Sturtevant, C., Oikawa, P. Y., Matthes, J. H., Verfaillie, J., and Baldocchi, D.: Using digital camera and Landsat imagery with eddy covariance data to model gross primary production in restored wetlands, *Agricultural and Forest Meteorology*, 237–238, 233–245, <https://doi.org/10.1016/j.agrformet.2017.02.020>, 2017.
- 565 Koesch, F., Sonnentag, O., Järveoja, J., Peltoniemi, M., Alekseychik, P., Aurela, M., Arslan, A. N., Dinsmore, K., Gianelle, D., Helfter, C., Jackowicz-Korczynski, M., Korrensalo, A., Leith, F., Linkosalmi, M., Lohila, A., Lund, M., Maddison, M., Mammarella, I., Mander, Ü., Minkkinen, K., Pickard, A., Pullens, J. W. M., Tuittila, E.-S., Nilsson, M. B., and Peichl, M.: Refining the role of phenology in regulating gross ecosystem productivity across European peatlands, *Global Change Biology*, 26, 876–887, <https://doi.org/10.1111/gcb.14905>, 2020.
- Körner Christian and Basler David: Phenology Under Global Warming, *Science*, 327, 1461–1462, <https://doi.org/10.1126/science.1186473>, 2010.
- 570 Larcher, W., Huber-Sannwald, E., and Wieser, J.: *Physiological Plant Ecology: Ecophysiology and Stress Physiology of Functional Groups*, Springer, 2003.
- Lees, K. J., Quaife, T., Artz, R. R. E., Khomik, M., and Clark, J. M.: Potential for using remote sensing to estimate carbon fluxes across northern peatlands – A review, *Science of The Total Environment*, 615, 857–874, <https://doi.org/10.1016/j.scitotenv.2017.09.103>, 2018.
- 575 Linkosalmi, M., Aurela, M., Tuovinen, J.-P., Peltoniemi, M., Tanis, C. M., Arslan, A. N., Kolari, P., Böttcher, K., Aalto, T., Rainne, J., Hatakka, J., and Laurila, T.: Digital photography for assessing the link between vegetation phenology and CO₂ exchange in two contrasting northern ecosystems, 5, 417–426, <https://doi.org/10.5194/gi-5-417-2016>, 2016.
- Linkosalo, T., Häkkinen, R., Terhivuo, J., Tuomenvirta, H., and Hari, P.: The time series of flowering and leaf bud burst of boreal trees (1846–2005) support the direct temperature observations of climatic warming, *Agricultural and Forest Meteorology*, 149, 453–461, <https://doi.org/10.1016/j.agrformet.2008.09.006>, 2009.
- 580 Lohila, A., Aurela, M., Hatakka, J., Pihlatie, M., Minkkinen, K., Penttilä, T., and Laurila, T.: Responses of N₂O fluxes to temperature, water table and N deposition in a northern boreal fen, *European Journal of Soil Science*, 61, 651–661, <https://doi.org/10.1111/j.1365-2389.2010.01265.x>, 2010.
- Lund, M., Christensen, T. R., Lindroth, A., and Schubert, P.: Effects of drought conditions on the carbon dioxide dynamics in a temperate peatland, 7, <https://doi.org/10.1088/1748-9326/7/4/045704>, 2012.
- 585 Maanavilja, L., Riutta, T., Aurela, M., Pulkkinen, M., Laurila, T., and Tuittila, E.-S.: Spatial variation in CO₂ exchange at a northern aapa mire, *Biogeochemistry*, 104, 325–345, <https://doi.org/10.1007/s10533-010-9505-7>, 2011.
- Meroni, M., Verstraete, M. M., Rembold, F., Urbano, F., and Kayitakire, F.: A phenology-based method to derive biomass production anomalies for food security monitoring in the Horn of Africa, null, 35, 2472–2492, <https://doi.org/10.1080/01431161.2014.883090>, 2014.
- 590 Migliavacca, M., Galvagno, M., Cremonese, E., Rossini, M., Meroni, M., Sonnentag, O., Cogliati, S., Manca, G., Diotri, F., Busetto, L., Cescatti, A., Colombo, R., Fava, F., Morra di Cella, U., Pari, E., Siniscalco, C., and Richardson, A. D.: Using digital repeat photography and eddy covariance data to model grassland phenology and photosynthetic CO₂ uptake, *Agricultural and Forest Meteorology*, 151, 1325–1337, <https://doi.org/10.1016/j.agrformet.2011.05.012>, 2011.
- 595 Migliavacca, M., Sonnentag, O., Keenan, T. F., Cescatti, A., O’Keefe, J., and Richardson, A. D.: On the uncertainty of phenological responses to climate change, and implications for a terrestrial biosphere model, 9, 2063–2083, <https://doi.org/10.5194/bg-9-2063-2012>, 2012.



- Morisette, J. T., Richardson, A. D., Knapp, A. K., Fisher, J. I., Graham, E. A., Abatzoglou, J., Wilson, B. E., Breshears, D. D., Henebry, G. M., Hanes, J. M., and Liang, L.: Tracking the Rhythm of the Seasons in the Face of Global Change: Phenological Research in the 21st Century, 7, 253–260, 2009.
- 600 Nordli, Ø., Wielgolaski, F. E., Bakken, A. K., Hjeltnes, S. H., Måge, F., Sivle, A., and Skre, O.: Regional trends for bud burst and flowering of woody plants in Norway as related to climate change, *International Journal of Biometeorology*, 52, 625–639, <https://doi.org/10.1007/s00484-008-0156-5>, 2008.
- Öquist, G. and Huner, N. P. A.: Photosynthesis of Overwintering Evergreen Plants, *Annu. Rev. Plant Biol.*, 54, 329–355, <https://doi.org/10.1146/annurev.arplant.54.072402.115741>, 2003.
- 605 Peichl, M., Sonnentag, O., and Nilsson, M. B.: Bringing Color into the Picture: Using Digital Repeat Photography to Investigate Phenology Controls of the Carbon Dioxide Exchange in a Boreal Mire, *Ecosystems*, 18, 115–131, <https://doi.org/10.1007/s10021-014-9815-z>, 2015.
- Peichl, M., Gažovič, M., Vermeij, I., de Goede, E., Sonnentag, O., Limpens, J., and Nilsson, M. B.: Peatland vegetation composition and phenology drive the seasonal trajectory of maximum gross primary production, *Scientific Reports*, 8, 8012, <https://doi.org/10.1038/s41598-018-26147-4>, 2018.
- 610 Peltoniemi, M., Aurela, M., Böttcher, K., Kolari, P., Loehr, J., Karhu, J., Linkosalmi, M., Tanis, C. M., Tuovinen, J.-P., and Arslan, A. N.: Webcam network and image database for studies of phenological changes of vegetation and snow cover in Finland, image time series from 2014 to 2016, 10, 173–184, <https://doi.org/10.5194/essd-10-173-2018>, 2018.
- Pudas, E., Leppälä, M., Tolvanen, A., Poikolainen, J., Venäläinen, A., and Kubin, E.: Trends in phenology of *Betula pubescens* across the boreal zone in Finland, *International Journal of Biometeorology*, 52, 251–259, <https://doi.org/10.1007/s00484-007-0126-3>, 2008.
- 615 Räsänen, A., Aurela, M., Juutinen, S., Kumpula, T., Lohila, A., Penttilä, T., and Virtanen, T.: Detecting northern peatland vegetation patterns at ultra-high spatial resolution, *Remote Sensing in Ecology and Conservation*, 6, 457–471, <https://doi.org/10.1002/rse2.140>, 2020.
- 620 Richardson, A. D., Jenkins, J. P., Braswell, B. H., Hollinger, D. Y., Ollinger, S. V., and Smith, M.-L.: Use of digital webcam images to track spring green-up in a deciduous broadleaf forest, *Oecologia*, 152, 323–334, <https://doi.org/10.1007/s00442-006-0657-z>, 2007.
- Richardson, A. D., Hollinger, D. Y., Dail, D. B., Lee, J. T., Munger, J. W., and O’Keefe, J.: Influence of spring phenology on seasonal and annual carbon balance in two contrasting New England forests, 29, 321–331, 2009.
- 625 Richardson, A. D., Keenan, T. F., Migliavacca, M., Ryu, Y., Sonnentag, O., and Toomey, M.: Climate change, phenology, and phenological control of vegetation feedbacks to the climate system, *Agricultural and Forest Meteorology*, 169, 156–173, <https://doi.org/10.1016/j.agrformet.2012.09.012>, 2013.
- Rinne, J., Tuovinen, J.-P., Klemetsson, L., Aurela, M., Holst, J., Lohila, A., Weslien, P., Vestin, P., Łakomiec, P., Peichl, M., Tuittila, E.-S., Heiskanen, L., Laurila, T., Li, X., Alekseychik, P., Mammarella, I., Ström, L., Crill, P., and Nilsson, M. B.: Effect of the 2018 European drought on methane and carbon dioxide exchange of northern mire ecosystems, *Philosophical Transactions of the Royal Society B: Biological Sciences*, 375, 20190517, <https://doi.org/10.1098/rstb.2019.0517>, 2020.
- 630 Sonnentag, O., Chen, J. M., Roberts, D. A., Talbot, J., Halligan, K., and Govind, A.: Mapping tree and shrub leaf area indices in an ombrotrophic peatland through multiple endmember spectral unmixing, 109, 342–360, <https://doi.org/10.1016/j.rse.2007.01.010>, 2007.
- 635 Sonnentag, O., Detto, M., Vargas, R., Ryu, Y., Runkle, B. R. K., Kelly, M., and Baldocchi, D. D.: Tracking the structural and functional development of a perennial pepperweed (*Lepidium latifolium* L.) infestation using a multi-year archive of webcam imagery and eddy covariance measurements, *Agricultural and Forest Meteorology*, 151, 916–926, <https://doi.org/10.1016/j.agrformet.2011.02.011>, 2011.
- 640 Sonnentag, O., Hufkens, K., Teshera-Sterne, C., Young, A. M., Friedl, M., Braswell, B. H., Milliman, T., O’Keefe, J., and Richardson, A. D.: Digital repeat photography for phenological research in forest ecosystems, *Agricultural and Forest Meteorology*, 152, 159–177, <https://doi.org/10.1016/j.agrformet.2011.09.009>, 2012.



- Tanis, C. M., Peltoniemi, M., Linkosalmi, M., Aurela, M., Böttcher, K., Manninen, T., and Arslan, A. N.: A System for Acquisition, Processing and Visualization of Image Time Series from Multiple Camera Networks, 3, <https://doi.org/10.3390/data3030023>, 2018.
- 645 Toomey, M., Friedl, M. A., Frohling, S., Hufkens, K., Klosterman, S., Sonnentag, O., Baldocchi, D. D., Bernacchi, C. J., Biraud, S. C., Bohrer, G., Brzostek, E., Burns, S. P., Coursolle, C., Hollinger, D. Y., Margolis, H. A., McCaughey, H., Monson, R. K., Munger, J. W., Pallardy, S., Phillips, R. P., Torn, M. S., Wharton, S., Zeri, M., and Richardson, A. D.: Greenness indices from digital cameras predict the timing and seasonal dynamics of canopy-scale photosynthesis, *Ecological Applications*, 25, 99–115, <https://doi.org/10.1890/14-0005.1>, 2015.
- 650 Turunen, J., Tomppo, E., Tolonen, K., and Reinikainen, A.: Estimating carbon accumulation rates of undrained mires in Finland—application to boreal and subarctic regions, *The Holocene*, 12, 69–80, <https://doi.org/10.1191/0959683602h1522rp>, 2002.
- Vrieling, A., Meroni, M., Darvishzadeh, R., Skidmore, A. K., Wang, T., Zurita-Milla, R., Oosterbeek, K., O'Connor, B., and Paganini, M.: Vegetation phenology from Sentinel-2 and field cameras for a Dutch barrier island, *Remote Sensing of Environment*, 215, 517–529, <https://doi.org/10.1016/j.rse.2018.03.014>, 2018.
- 655 White, M. A. and Nemani, R. R.: Canopy duration has little influence on annual carbon storage in the deciduous broad leaf forest, *Global Change Biology*, 9, 967–972, <https://doi.org/10.1046/j.1365-2486.2003.00585.x>, 2003.
- Wingate, L., Ogée, J., Cremonese, E., Filippa, G., Mizunuma, T., Migliavacca, M., Moisy, C., Wilkinson, M., Moureaux, C., Wohlfahrt, G., Hammerle, A., Hörtnagl, L., Gimeno, C., Porcar-Castell, A., Galvagno, M., Nakaji, T., Morison, J., Kolle, O., Knohl, A., Kutsch, W., Kolari, P., Nikinmaa, E., Ibrom, A., Gielen, B., Eugster, W., Balzarolo, M., Papale, D., Klumpp, K., 660 Köstner, B., Grünwald, T., Joffre, R., Ourcival, J.-M., Hellstrom, M., Lindroth, A., George, C., Longdoz, B., Genty, B., Levula, J., Heinesch, B., Sprintsin, M., Yakir, D., Manise, T., Guyon, D., Ahrends, H., Plaza-Aguilar, A., Guan, J. H., and Grace, J.: Interpreting canopy development and physiology using a European phenology camera network at flux sites, 12, 5995–6015, <https://doi.org/10.5194/bg-12-5995-2015>, 2015.
- Wipf, S.: Phenology, growth, and fecundity of eight subarctic tundra species in response to snowmelt manipulations, *Plant Ecology*, 207, 53–66, <https://doi.org/10.1007/s11258-009-9653-9>, 2010.
- 665 Wipf, S. and Rixen, C.: A review of snow manipulation experiments in Arctic and alpine tundra ecosystems, *POLAR*, 29, 95–109, <https://doi.org/10.3402/polar.v29i1.6054>, 2010.